MDPI

Article

Effect of Manufacturing Inaccuracies to the Wake past Asymmetric Airfoil by PIV

Daniel Duda [1,†,‡], Vitalii Yanovych [1,2,‡], Volodymyr Tsymbalyuk [1,†] and Václav Uruba [1,2]

[1] University of West Bohemia, Univerzitní 22, Pilsen, Czech Republic; dudad@kke.zcu.cz
[2] Institute of Thermomechanics, Czech Academy of Sciences, Dolejškova 5, Prague, Czech Republic; uruba@kke.zcu.cz
* Correspondence: dudad@kke.zcu.cz; Tel.: +420-377-638-146
† Current address: Affiliation 3
‡ These authors contributed equally to this work.

Abstract: The effect of manufacturing geometry deviations to the flow past NACA 64(3)-618 asymmetric airfoil is studied. This airfoil is 3D printed according to the coordinates from public database. An optical high-precision 3D scanner GOM Atos measures the difference from the idealized model. Based on this difference, another model is prepared with physical output closer to the ideal model. The velocity in the near wake ($0 - 0.4$ chord) is measured by using the Particle Image Velocimetry (PIV) technique. This work compares the wakes past three airfoil realizations, which differ in their similarity to the original design (none of the realizations is identical to the original design). The chord-based Reynolds number ranges from $1.6 \cdot 10^4$ to $1.6 \cdot 10^5$. The ensemble average velocity is used for determination of the wake width and for roughly estimation of the drag coefficient. The lift coefficient is measured directly by using force balance. We discuss the origin of turbulent kinetic energy in terms of anisotropy (at least in 2D) and the length-scales of fluctuations across the wake. The spatial power spectral density is shown. Autocorrelation function of cross-stream velocity detects the regime of von Karmán vortex street at lower velocities.

Keywords: Particle Image Velocimetry ; Wake ; 3D scanning ; NACA 64-618 ; Turbulent kinetic energy ; Spectrum

Citation: Duda, D.; Yanovych, V.; Tsymbalyuk, V.; Uruba, V. PIV past airfoils of different quality. *Energies* **2021**, *1*, 0. https://doi.org/

Received:
Accepted:
Published:

1. Introduction

The fluid flow is a highly non-linear problem without reasonable solution up to nowadays. One of the general effects of non-linearity is the unpredictable response to even a small perturbations or changes of the boundary conditions. The scale of possible responses to a small geometry perturbation ranges from almost zero effect, trough a linear response up to a complex change of flow state. The famous *butterfly effect* represents this behavior on the example of a small butterfly which *can* switch the evolution path of the turbulent system [1]. As there is a large number of such micro-events, the evolution path of the entire system is unpredictable. But, the statistical properties can be predicted quite reasonably. This feature is used in modern *computational fluid dynamics*, which does not solve the non-linear Navier-Stokes equations on a fine mesh with resolution of Kolmogorov length-scale, but it solves only much larger cells with direct link to the geometry of the boundary conditions under assumption, that the behavior at smaller scales follows some of the *turbulence models*.

The relatively low-cost computational fluid dynamics attacks the position of thorough experiments on the place of industrial design and optimization. But the computational methods need validation and verification [2], which is mainly based on the comparison with an appropriate experiment, which does not need to fit in all parameters, but, at least, the main geometrical and fluid properties might be met. And here comes

the problem with geometry – the object used in the experimental study is different from the desired design used in the computational approach. As the quality needs to increase, even smaller deviations between numerical and experimental results can be accepted. As the experiment has an aura of the truth, the mathematicians sweat blood developing even better and more accurate models in order to fit the experimental data measured with boundary conditions known only approximately.

In this study, we use a high-quality contact-less 3D optical scanner to measure the real geometry of boundary conditions (of course, with some uncertainty connected with each measurement technique) and compare the flow field past an airfoil produced at three levels of accuracy – first variant represents the naive approach, we send to the 3D printer just the coordinates obtained from public database [3]. If we have not got the 3D optical scanner, our study ended here declaring "'we measured flow in the near wake past airfoil..."'. However, the 3D scan discovered discrepancies from the ideal geometry, therefore we try to prevent them by manipulating the geometry in a such way, that the outcome is closer to the ideal case. This step is repeated creating two more variants closer and closer to the ideal geometry. Anyway, the best product is still different from the ideal geometry used in the processes of numerical optimization.

There is only very little other studies about the manufacturing inaccuracies and they are numerical only. Our study is experimental and it compares really created models. A disadvantage is, that there does not exists the ideal geometry in reality, hence we can compare only different levels of manufacturing attention.

1.1. Some recent literature concerning this problem

Moreno-Oliva and coworkers [4] used the Laser Triangulation Technique to measure the real profile of a NACA0012 and FX 61-137 airfoil, one realization of the NACA0012 has been commercially made of metal, the second has been 3D printed by the authors from PLA, the profile FX 61-137 was measured at real wind turbine blade at several heights. They used the measured profiles as an input into the Xfoil software [5] together with the theoretical profiles. They report a significant decrease of performance of the real wind turbine profiles when compared with the ideal geometry.

Ravikovich et al. [6] performed an optimization of fan blades with real geometry deviations from airfoil geometry. Their algorithm simultaneously solves mechanical integrity problems and aerodynamic stability of the flow. The geometry data measured at cold conditions are transformed via numerical simulation into hot conditions, which allows to estimate the influence of measured geometry to final fan parameters.

The effect of even small geometry modifications in turbine stator blades is studied by Klimko and Okresa [7]. The modifications in stator wheel affects the reaction and efficiency of the entire stage. Data like the just mentioned ones are used in numerical optimization [8] of developed new stage.

Winstroth and Seume [9] studied numerically the effect of several artificial geometry deviations on four wind turbine airfoils. The geometry deviations cover mold tilt towards leading or trailing edge, step changes at certain position, sine wave placed at several positions on both pressure and suction side or at leading edge, and thickening of the profile – in total 40 modifications of four different airfoil profiles used in the studied wind turbine. They found that the worst deviation (in terms of energy production) is the tilt towards leading edge; they found also some cases with positive impact.

The structure of our article is as follows: first we describe the methods including 3D printing, 3D optical scanning and Particle Image Velocimetry used to measure 2D velocities within a square area past the trailing edge. This paper focuses to data at zero angle of attack, some data at angle of attack $\alpha = 10^\circ$ are in the appendix. The ensemble average stream-wise velocity, the path of wake centerline and the wake width based on average stream-wise velocity are shown. The lift coefficient is impossible to determine on the basis of PIV data, therefore a simple balance is introduced and the lift at zero angle of attack and at several Reynolds number is measured. The turbulent kinetic energy

is explored discussing, if it is produced by fluctuations in stream-wise or cross-stream velocity component. The length-scale of fluctuations is explored by unique method developed at the University of West Bohemia in Pilsen. The autocorrelation function reveals the periodicity at low velocities and the decay of integral length-scale at larger ones.

2. Materials and methods

2.1. 3D printer

We used a commercially available 3D printer `Prusa Mk 2.5`. It uses the FDM (Fused Deposition Modeling) printing technology [10]. The used material is the thermoplastic polymerized lactic acid PLA [11]. The nozzle temperature was 230 °C, the height of a single layer 0.15 mm. The 3D printed airfoils are used mainly for testing and development purposes. At the current stage, 3D printing technology is not suitable for industrial manufacturing. However, it is important to know the impact of the typical 3D printing shortcomings.

2.2. 3D scanner

The optical 3D scanning method FPS (Fringe Projection Scanning [12]) is based on projecting light periodic stripes onto the surface [12,13] and the variations of their phase is used to estimate the variations of height across the measured surface. The commercial 3D optical scanner `GOM Atos Core` [14] is used in our study. Mendřický [15] measured accuracy of a such scanner in dependence on the calibration and the optical matteness of measuring surface of standard spheres. He found that the accuracy is in order of micrometers, matte coating adds around 10^{-5} m, while just an old calibration can change measured results systematically by around $2 \cdot 10^{-5}$ m. Li et al. [13] found that the ambient light has only small effect on the results, while Vagovský et al. [16] states that even the size of scanned object influences the accuracy due to the focus blur. Measuring volume of our scanner is 300 cm^3, thus the airfoil of height 12.5 cm is small for such volume, but still, our object size is much closer to the measured volume than in the case explored by Vagovský [16]. We did not used the matte coating because we used white PLA material; on the other hand, we had to paint it to black before the PIV measurement, which uses intense laser light, and we did not measured the thickness added by this painting.

2.3. Model

The coordinates of NACA 64-618 airfoil were got from a public database Airfoiltools.com [3]. This airfoil is frequently used at tips of the wind turbines [17] and have a reasonable lift even at high angles of attack (which is valid only for larger Reynolds numbers, as will be shown later). The trailing edge of this airfoil is sharp and it points towards the high pressure side, see the black line in Figure 1. First, this airfoil was 3D printed just according the point coordinates obtained from the public database [3]; this first naive realization is denoted A. Then a high-precision 3D optical scanner `GOM Atos` [18] is used to measure the deviation from the ideal geometry, see Figure 1. There exists a huge systematic printing error – the missing trailing edge, see Figure 1c. This is caused by the finite thickness of the extrusion line, which does not fit into the too thin walls and the program for generating the g-code does not let the extruder moving into that locations. The trailing edge is shorter by almost 3 mm, which is 3.7% of the chord length!

A next step was to create the trailing edge thicker in order to fill it with at least some material. This was done by Minkowski sum [19] of the airfoil profile with an circle of radius 0.2 mm. This way leads to too large thickening of the entire model, but the trailing edge is still shorter than it should be. This blind way is not reported here. Next trial, denoted B, is obtained by artificial manipulation with the profile points at the trailing edge combined with the Minkowski sum with circle of radius 0.1 mm. Now, the trailing

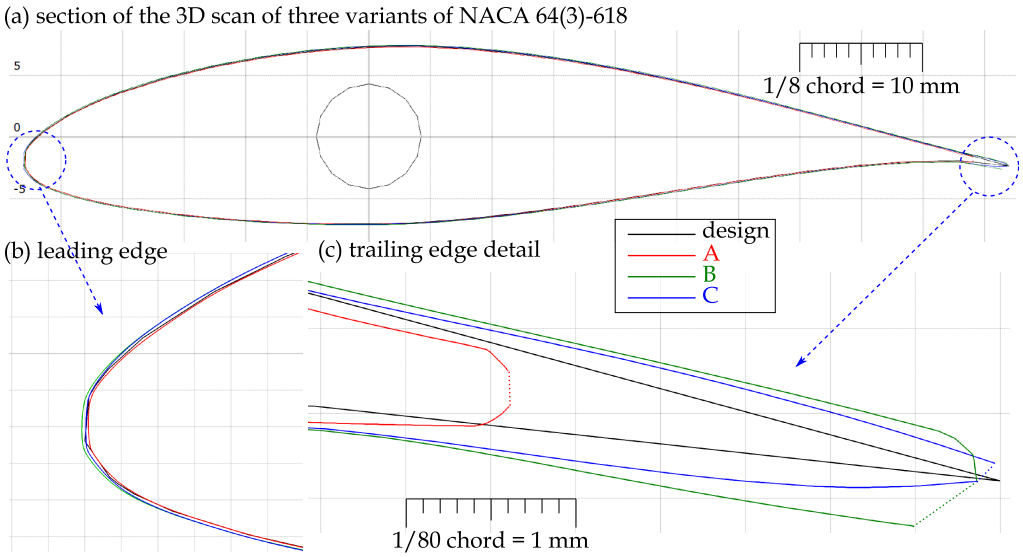

Figure 1. Comparison of 3D scans of three manufactured realizations of the NACA 64-618 airfoil, which is depicted by solid black line. The production details are in text. Panels (b) and (c) zoom the details of leading and trailing edge respectively.

Table 1: Dimensions of the studied airfoil realizations compared with the ideal case denoted CAD in first column. The blockage ratio of the wind tunnel is the ratio of blocked projection are to the total cross-section area (125 × 125 mm), it is calculated from the *caliper* approach, i.e. the distance of plane touching suction side to second plane touching the pressure side, when their normals are locked to the y-axis.

	Unit	CAD	A	B	C
Chord length c	[mm]	80.00	77.01	79.83	80.08
Profile thickness – maximum inscribed circle	[mm]	14.36	14.34	14.55	14.47
Profile thickness – caliper along y-axis	[mm]	14.44	14.41	14.63	14.55
Blockage ratio	[%]	11.55	11.53	11.70	11.64

edge is shorter by around 0.2 mm only. On the other hand, the trailing edge displays a large radius of around 0.3 mm.

The best result is obtained by using Minkowski sum with circle of 0.1 mm radius, adding new points into the trailing edge area expanding it over the ideal edge. After printing, the model was polished manually in order to sharp the trailing edge. As a side effect, the surface of this last realization, denoted C, is smoother than the previous ones. The problem with manual polishing is that (i) it is a non-repeatable procedure, and (ii) it is too expensive for possible industrial use.

2.4. Wind tunnel

University of West Bohemia in Pilsen has got multiple wind tunnels [20,21]. But, due to the laser safety requirements, we are limited with the use of PIV method to the "small" wind tunnel [22] with transparent test-section of length 400 mm, and cross-sectional size 125 × 125 mm. It is an open low-speed wind tunnel driven by the radial fan at the tunnel inlet. The smallest stable velocity used in this study is $U_{\mathrm{ref}}^{\mathrm{min}} = 3.1\,\mathrm{m/s}$; the largest used reference velocity is 30.6 m/s. The working fluid is atmospheric air of temperature around 20 °C, the actual humidity was not measured.

The Reynolds number used in this study is based on the above mentioned reference velocity U_{ref}, which fits the incoming velocity in the case of empty test section of the

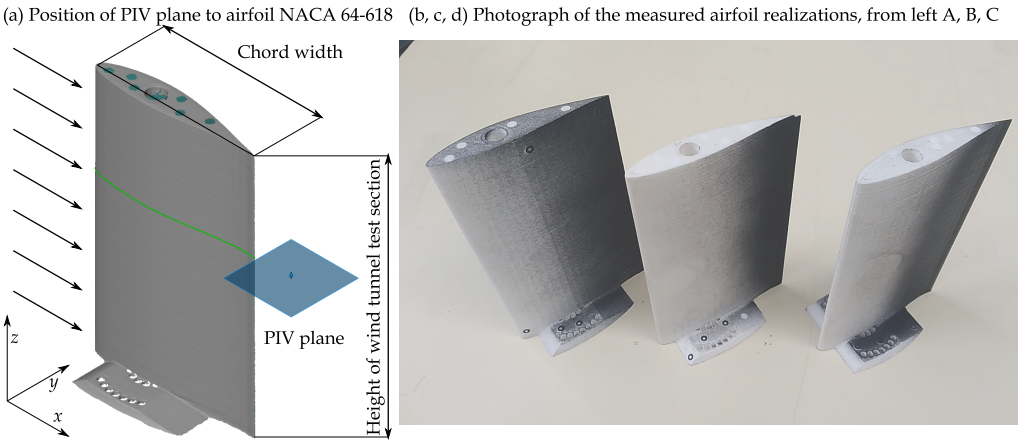

Figure 2. (a) Position of the area studied by using Particle Image Velocimetry depicted as a blue square just behind the trailing edge of the airfoil. The PIV area is a square of side 32 mm $= 0.4c$. The estimated thickness of the illuminated plane is ~ 1 mm. The laser light comes from counter stream direction. (b - d) Photograph of the 3D printed realizations of the airfoil. Their trailing parts are blacked in order to suppress the laser reflections.

wind tunnel. As the length-scale for Reynolds number, the planned chord length of the airfoil is used. It is a constant $c = 80$ mm. Note, the real chord slightly differs among realizations A, B and C (see Table 1 for more details). The range of Reynolds numbers used in this study spans one order of magnitude from $1.63 \cdot 10^4$ (corresponding to $U_{\text{ref}} = 3.1$ m/s) up to $1.63 \cdot 10^5$, where $U_{\text{ref}} = 30.6$ m/s.

2.5. Particle Image Velocimetry

The method Particle Image Velocimetry [23] visualizes the wake structure in a small area just behind the airfoil, see Figure 2(a). This method is based on optical observation of movement of small particles carried by the studied fluid. In our case, the particles are droplets of `Safex` of diameter in the order of micrometers. When the droplets are small enough, they follow the fluid motion because the inertial forces scale with particle volume, i.e. as $\sim r^3$, while the viscous forces unifying the motion of particles and fluid scale with particle surface, i.e. as $\sim r^2$. These particles are illuminated in a single plane by using a solid-state pulse laser `New Wave Solo` using the second harmonics of wavelength $\lambda = 532$ nm (corresponding to green color). The single shot energy is 0.5 J and its duration is 5 ns, thus the peak power is 100 MW. The laser produces a pair of pulses separated by time-interval $10^{-5} - 10^{-4}$ s in dependence on the flow velocity. The laser beam is defocused by using a cylindrical optics in order to illuminate the plane. The camera is oriented perpendicularly to this plane and focused into it. The `Mk II Flow Sense` CCD camera has resolution of 2048×2048 pixels; this camera is able to resolve both pulses of the laser into a pair of expositions. The obtained pairs of photographs of particles are processed by using the `Dantec Dynamic Studio` software[1]. The vector fields contain 64×64 vectors, a single grid point covers area of 0.53×0.53 mm^2 corresponding to $6.65 \cdot 10^{-3}$ times the chord length c. The analysis continues by using our custom-made software: one grid point is removed from each side getting resolution 62×62 vectors, because the vectors at the edge of the field of view are

[1] Details for readers familiar with this software: (1) first 5 frames are removed from each movie, (2) the minimum of image ensemble is calculated by using `Image Min/Max` function, (3) this minimum is subtracted from each image in the ensemble by using the `Image Arithmetic` function, (4) the velocity vectors are calculated by using the `Adaptive PIV` function with parameters: grid step size 32, minimum IA size 32, maximum IA size 32, validation based on universal outlier detection over neighborhood 5×5, normalization 0.1, acceptance limit 2.0, the algorithm adapts to the particle density with particle detection limit of 5 to the desired number of 10 particles per IA; it adapts IA shape to velocity gradients with $|Ux|, |Vx|, |Uy|, |Vy| \leq 0.1$ and $\sqrt{Ux^2 + Vx^2 + Uy^2 + Vy^2} \leq 0.2$, the convergence limit is 0.01 pixel and the maximum number of iterations is 10. (6) The last step within the Dantec software is the export via `Numeric Export` function.

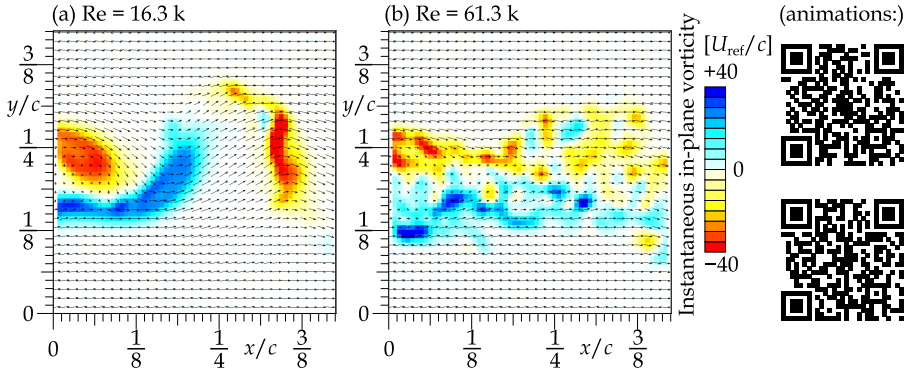

Figure 3. The example of instantaneous velocity fields at chord-based Reynolds numbers $1.63 \cdot 10^4$ (a) and $6.13 \cdot 10^4$ (b), both at zero angle of attack. Only every second velocity vector is displayed. The color in background represents z-component of vorticity $\omega = \nabla \times \vec{u}$. The QR-codes link to http://home.zcu.cz/~dudad/PIV_uplav_3ms.gif and http://home.zcu.cz/~dudad/PIV_uplav_12ms.gif, which show pair of photos used for drawing this figures.

not trustworthy, as there is relevant number of particles leaving or entering the field of view during the *time between laser pulses*. Second step is to filter out the snapshots, whose small-scale energy content is significantly greater than the average of the ensemble. This procedure serves for removing rough errors, whose smallest-scale energy content is typically large. This method is in more details described in our previous article [24]. In fact, current data have reasonable quality, therefore, this procedure removes at least one snapshot only for 40 % of datasets. The example of obtained instantaneous velocity field is displayed in Figure 3.

2.6. Lift force measurement

Wind-tunnel balance is designed to measure the lift force L on the airfoil. The basis of the balance is a resiliently suspended movable table. Elastic suspension created with 4 parallel flexible elements. The elastic suspension has the lowest stiffness in the direction of the force L and in all other directions the stiffness is an order of magnitude higher. The displacement of the table is measured by an eddy-current sensor which responds to the distance to the steel target. Unwanted vibrations are dampened by eddy-currents in the copper sheet as it moves near to the neodymium super magnet. The output of the sensor is calibrated by a known force created by using a calibration weight in the lift direction.

3. Results and discussion

3.1. Zero angle of attack – average velocities

The average stream-wise velocity component for four different Reynolds numbers is displayed in Figure 5. In that figure, the spatial distribution for each case (velocity and airfoil realization) is plotted as a colormap. The direct comparison of isotachs (contour lines of velocity) for each product is plotted in a single panel in order to see the differences among those products. Figure 6 shows the profile of average stream-wise velocity at distance 10 mm $= 1/8c$ past the trailing edge. This plot contains less information than the previous one, but this information is organized in a different manner in order to catch the differences better.

First look to figures 5 and 6 reveals, that the largest difference occurs at Reynolds number $4.08 \cdot 10^4$ (denoted 40.8k, where k plays for $\cdot 10^3$ as a standard multiplicator of SI system). This Reynolds number is close to a critical Reynolds number of transition between wake dominated by von-Kármán vortex street [25] and the wake dominated by continuous boundary layers developed along the airfoil, as will be apparent from next

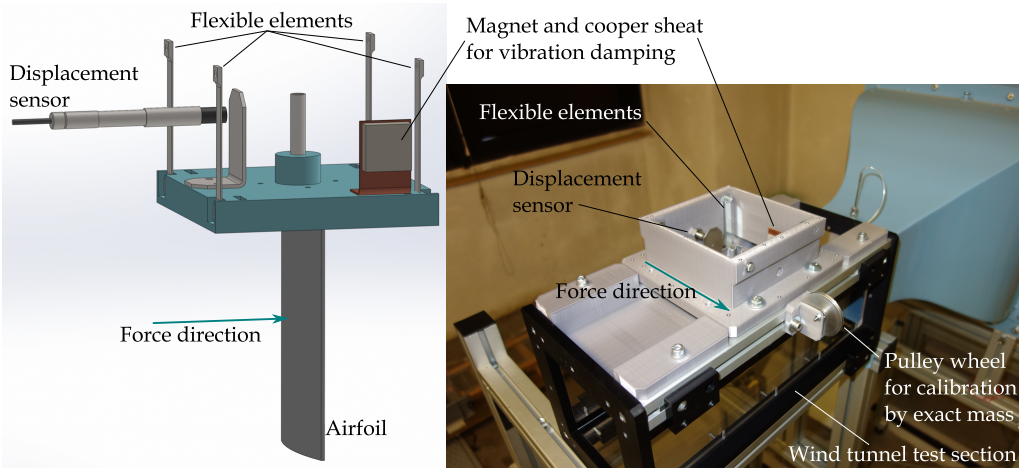

Figure 4. Sketch and photograph of the balance used for lift force measurement. The metallic flexible elements are connected to the wind tunnel walls at their upper end. The airfoil is reinforced by using an aluminum tube, which connects the airfoil to the movable table as well. The eddy-current sensor is used to electrically measure the displacement of entire table.

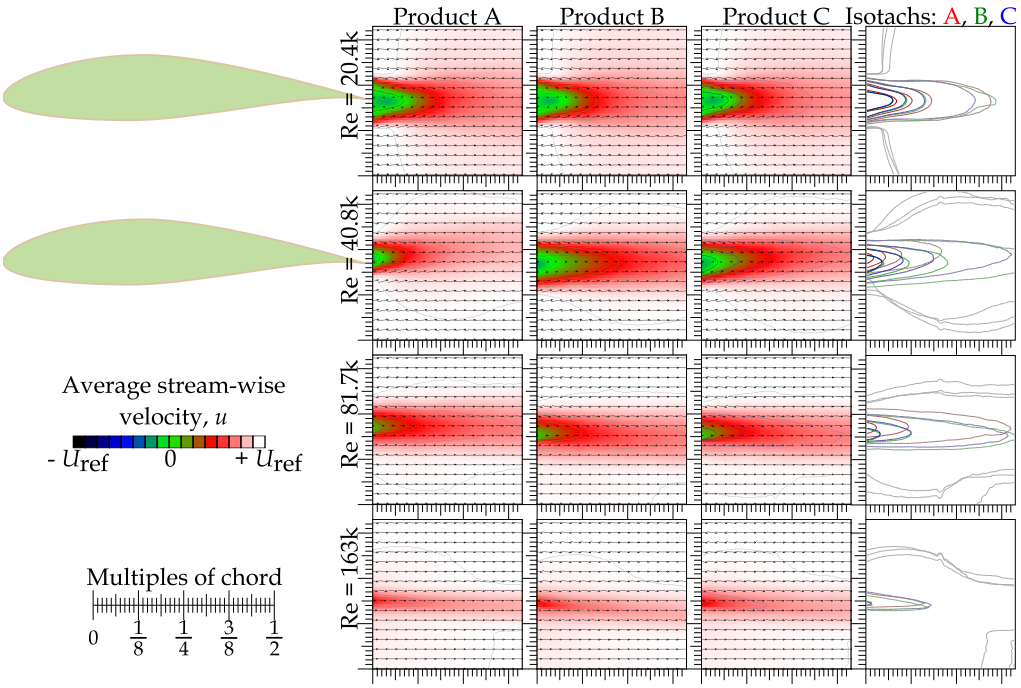

Figure 5. First three columns show the map of average stream-wise velocity u normalized by the reference velocity U_{ref} past the slightly different samples A, B and C. Fourth column displays isotachs together. The green tips in the left edge of figure represent the positions of airfoil trailing edge. Reynolds number is based on chord length and the reference velocity. The reference velocity is measured in the empty wind tunnel under otherwise similar condition. Angle of attack $\alpha = 0°$ in all panels.

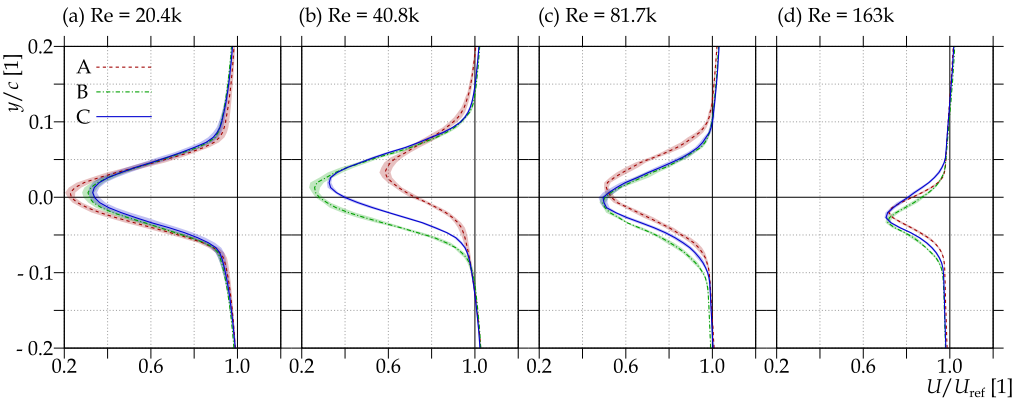

Figure 6. The cross-stream profile of average stream-wise velocity $\langle u \rangle$ at stream-wise distance 10 mm $= 1/8c$ past the trailing edge. Angle of attack $\alpha = 0°$ in all panels. The uncertainty is displayed via the area.

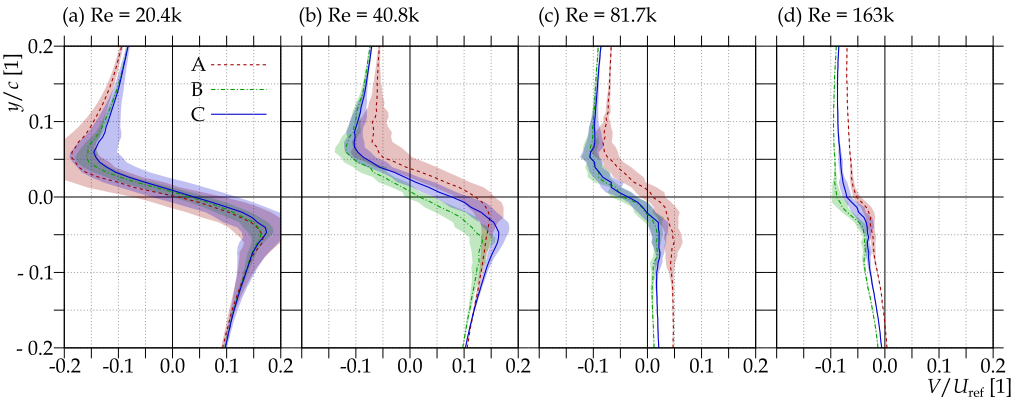

Figure 7. The cross-stream profile of average cross-stream velocity $\langle v \rangle$ at stream-wise distance 10 mm $= 1/8c$ past the trailing edge. Angle of attack $\alpha = 0°$ in all panels.

figures analyzing turbulent kinetic energy (mainly the ratio $\sigma[v]/\sigma[u]$ in Figure 15). As it was mentioned above, the variant A is slightly smaller than B and C, which both are expanded by Minkowski sum with circle of radius 100 mum. Therefore, it is natural to expect, that the *real* Reynolds number for those variants is slightly larger than that for variant A, thus the transition occurs at slightly smaller velocities.

The next largest discrepancy lies in the *position* of the wake past variant A. It is best apparent at Reynolds number $8.17 \cdot 10^4$, although at others it applies as well. This shift is caused by the missing trailing edge of the variant A, see Figure 1. As the trailing edge is slanted towards the pressure side (direction down in the figures), the entire airfoil ends upper (in figures) and thus the entire wake is shifted up. One may ask, why this shift is less apparent at the lower Reynolds number? We think, that it is due to the different mechanism of wake creation – the von Kármán vortex street is formed due to Kelvin-Helmholtz instability of the shear layer between the fluid, which passes far from the obstacle, and between the fluid, which is slowed by the presence of the obstacle. But this difference starts at the *leading edge*, which is much more similar among different airfoil variants, see Figure 1(b).

3.2. Balance measurement of lift coefficient

According to the momentum balance principle, the lift force acting one direction has to deflect the fluid motion in opposite direction. However, the true integration of the momentum deflected needs the knowledge of the flow field around the entire airfoil,

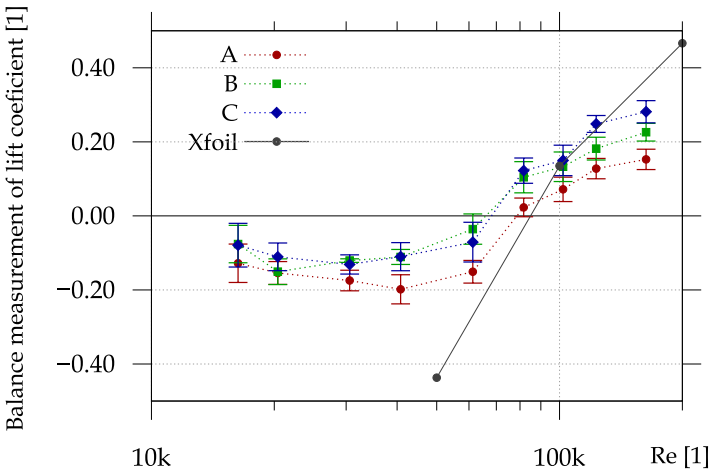

Figure 8. Balance measurement of the lift coefficient. The theoretical results for ideal geometry are displayed as well. Angle of attack $\alpha = 0°$.

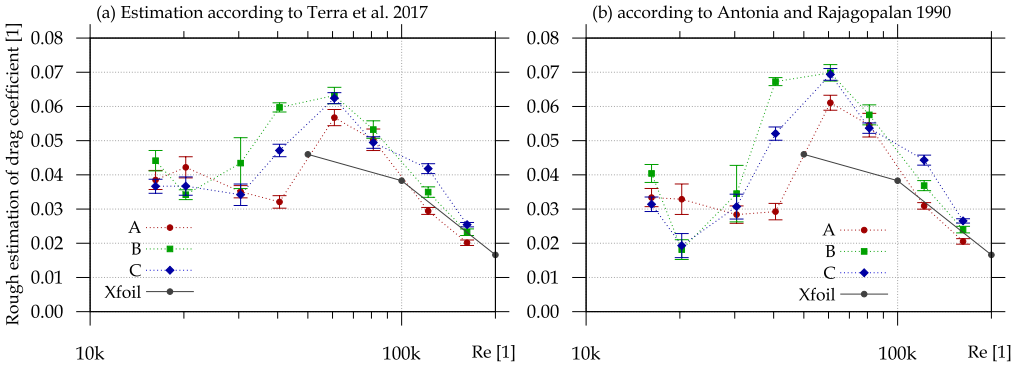

Figure 9. Rough estimation of the drag coefficient based only on the momentum deficit and stress term, the pressure term is ignored. Black points denote data obtained from public database Airfoiltools [3] calculated by using the Xfoil [5,26,27] for the $N_{\text{crit}} = 9$. Angle of attack $\alpha = 0°$ in all panels.

which is not available. In order to get some information about the lift, which is anyway the crucial feature of any airfoil, we measured it by using a force balance equipped with four flexible metal elements in order to allow deformation in a single direction only, see figure 4. The resulting lift coefficient is shown in Figure 8 for angle of attack equal to 0° and for Reynolds numbers in the same range as used for the PIV measurement. This figure shows a reasonable match with the prediction by the Xfoil algorithm [5,26,27] at Reynolds number 10^5, but the values are heavily different at lower and higher velocities. Differences among airfoil realizations shows, that the A variant performs lowest lift as expected. The geometrically best airfoil C has the best aerodynamic performance. Interestingly, the A airfoil has larger negative values of lift at low velocities. The large errors reported here are cause by the unwanted oscillations at higher velocities (despite the damping by using highly-conductive cooper and a strong magnet). At smaller values, the large error is caused simply be the uncertainty of the displacement sensor and of the Analog-Digital converter, because the forces are by two orders of magnitude smaller than the range adapted to fit the expected forces at largest velocities.

3.3. Rough estimation of drag coefficient

The time-average drag force $\langle F_D \rangle$ can be roughly estimated according to the principle of momentum balance:

$$\frac{\langle F_D \rangle}{\rho} = \int_{\text{wake}} (U_\infty - \langle u \rangle)\langle u \rangle \mathrm{d}S - \int_{\text{wake}} \sigma^2[u]\mathrm{d}S + \int_{\text{wake}} (p_\infty - \langle p \rangle)\mathrm{d}S, \tag{1}$$

where U_∞ is the velocity in the unperturbed state, see the work of Terra et al. [28,29] for more details; $\mathrm{d}S$ is the surface element across the wake and $\sigma^2[u]$ is the variation of u. This fluctuation term originates from the averaging of Reynolds-decomposed momentum balance equation and it *decreases* the resulting force. The calculation of the last term with static pressure p is rather complicated [30] as all components of velocity gradient are needed to be known in order to integrate the pressure Poisson equation [31]. Terra et al. [28] used tomographic PIV in order to get this term and they found that, fortunately, the pressure term is important only up to the recirculation zone, it disappears downstream, see Figure 13 in [28]. This observation allows us to ignore this term and estimate the drag force only by using the measured spatial velocity distribution as

$$\frac{\langle F_D(x) \rangle}{\rho H} \approx \int_{\text{FoV}} (U_0 - \langle u(x) \rangle)\langle u(x) \rangle - \sigma^2[u(x)] \quad \mathrm{d}y, \tag{2}$$

where the integration is performed along y-direction in the measured two-dimensional FoV at fixed x-position, which is far enough to ignore the pressure term. In our case $x = 0.4c$ is chosen (i.e. the most downstream position within our FoV). H is the height of prismatic airfoil. The background velocity U_∞ is replaced by the background U_0 of Gaussian fit of the velocity profile (equation (5)).

There exist another approach to estimate the drag coefficient by using the spatial distribution of measured velocity across the wake. Antonia and Rajagopalan [32] offer an alternative procedure including the transverse velocity fluctuations as well

$$\frac{\langle F_D \rangle}{\rho H} \approx \int_{\text{FoV}} (U_0 - \langle u \rangle)\langle u \rangle + \sigma^2[u] - \sigma^2[v] \quad \mathrm{d}y. \tag{3}$$

The fluctuations in stream-wise direction are though to increase the drag force, while in Terra's definition (2), they decrease the force. At higher velocities, the estimations are very similar both dominated by the first term of the average momentum deficit; at middle Reynolds numbers, the stream-wise fluctuations are more important and the Antonia's approach gives larger values than the Terra's one. At low Reynolds numbers, the wake is dominated by transverse fluctuations associated with the vortex street decreasing the drag, which is revealed when using the Antonia's formula. The later formula is widely used in literature; e.g. Zhou et al. [33] compared the direct force measurement by using load-cell with this formula applied to the transverse profiles measured by using Laser Doppler Anemometry (LDA) technique. Mohebi et al [34] uses this formula to study the flow past a flat plate at high angles of attack.

3.4. The wake width and centerline

By using the spatial distribution of average stream-wise velocity, the wake centerline can be determined. It is a set of points, where the stream-wise velocity component is minimal, i.e. the velocity deficit $u_d = U_{\text{ref}} - \langle u \rangle$ is maximal. The maximum or minimum are by zero derivation:

$$\frac{\mathrm{d}\langle u \rangle}{\mathrm{d}y} = 0 \tag{4}$$

The respective isolines for different Reynolds numbers are shown in Figure 10. The main line along the axis shows the wake centerline, where the average stream-wise velocity is minimal. However, there are visible another structures as well: at low Re, there are

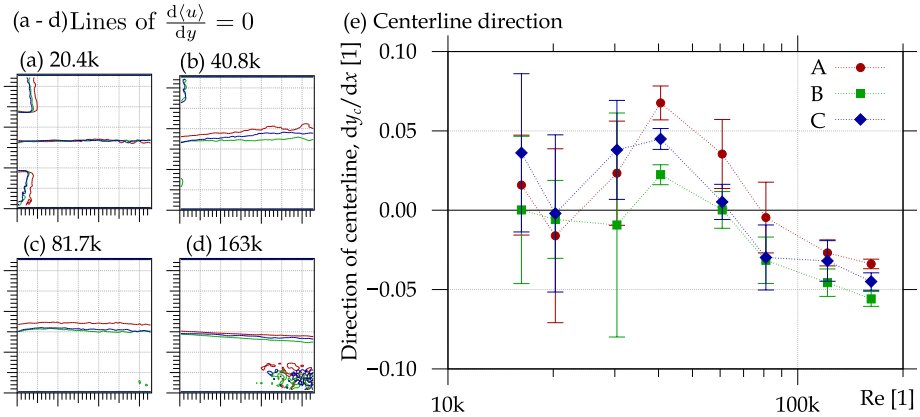

Figure 10. (a – d) Lines of extrema of $\langle u \rangle$ along cross-stream direction (y). The number in top right corner of each panel is chord-based Reynolds number and k denotes $\cdot 10^3$. (e) Direction of centerline as a function of Reynolds number. It is obtained as a linear fit of the coordinates of minima of transverse profiles. Angle of attack $\alpha = 0°$ in all panels.

depicted the maxima caused by the acceleration along the airfoil enforced by the mass balance. At highest Re, some noise appears in the bottom right corner.

The wake width δ_w can be calculated by using multiple approaches [35] in dependence which physical property has to be explored. [35] shows that for comparison purposes the most suitable wake width is determined as twice the σ-parameter of a Gaussian function fitted to the ensemble-average stream-wise velocity profile:

$$u(y) \approx G(y) = U_0 - u_d e^{-\frac{(y-y_c)^2}{2\sigma}}, \tag{5}$$

where U_0 plays a role of a background, u_d is the deficit velocity, y_c is the y-coordinate of centerline and σ can be interpreted as half of the wake width. The Gaussian function fits well, as suggested e.g. by [36] (where the wake past circular cylinder is explored by using Acoustic Doppler Velocimetry.) The dependence of $\delta_w = 2\sigma$ on the stream-wise distance from the airfoil trailing edge is displayed in Figure 11 together with the deficit velocity u_d for each stream-wise distance x. We see that the wake width increases with distance, however, at small Reynolds number, there is a minimum of the wake width. This minimum would be more apparent when taking into account the fluctuations as shown in [35]. The observed growth of wake width is approximately linear, but, according to Eames [36], the transition to $\sim x^{0.5}$ growth can be expected downstream. The power of wake width growth rate is locked with the power of velocity deficit decrease by the conservation of momentum deficit within the wake. However, this rule do not need to be valid in the near wake, where the pressure field plays its own role.

The evolution of δ_w with Re at fixed distance $x = 0.4c$ is plotted in Figure 12 as well as the wake growth rate a and the velocity deficit at fixed distance.

3.5. Turbulent kinetic energy

The turbulent kinetic energy (TKE) is calculated as

$$E_T(\vec{x}) = \frac{1}{2}\left\langle u^2(\vec{x}) - \langle u(\vec{x})\rangle^2 + v^2(\vec{x}) - \langle v(\vec{x})\rangle^2 \right\rangle, \tag{6}$$

where u and v are the stream-wise and cross-stream velocity components measured by using PIV, $\vec{x}$ is the position within the field of view and the sharp brackets $\langle\cdot\rangle$ denote the averaging over the ensemble. Note that this definition of TKE contains the in-plane velocity components only, therefore its value is roughly underestimated by the entire z-component term. The level of underestimation may vary with the regime of flow past the

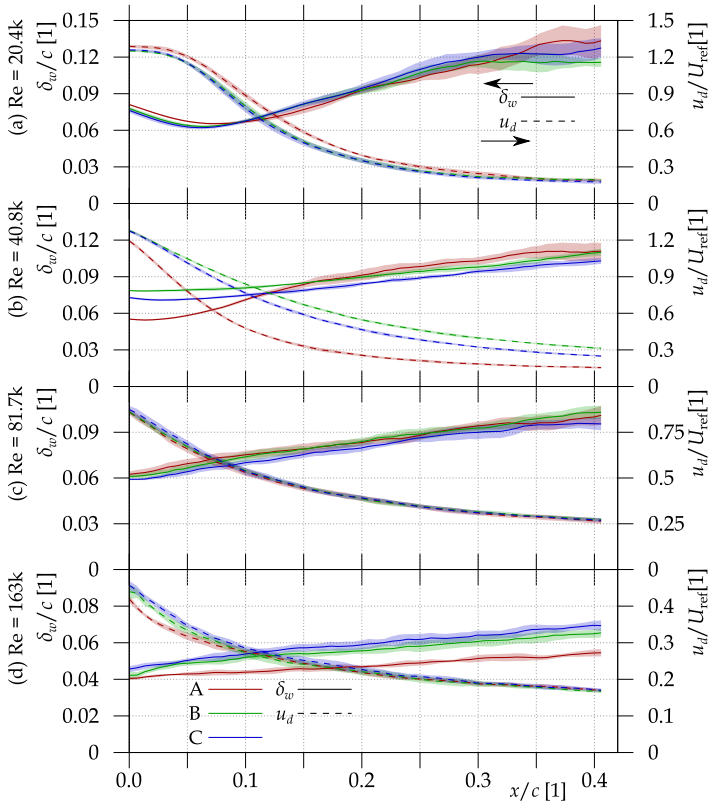

Figure 11. Solid lines indicate the wake width as a function of distance past the airfoil trailing edge, x; the corresponding axis is on the left-hand-side of the plots. Dashed lines represent the maximum deficit velocity as a function of x; the axes for these values are on the right-hand-side of the plots. Different panels contain data at different Reynolds numbers and angle of attack $\alpha = 0°$.

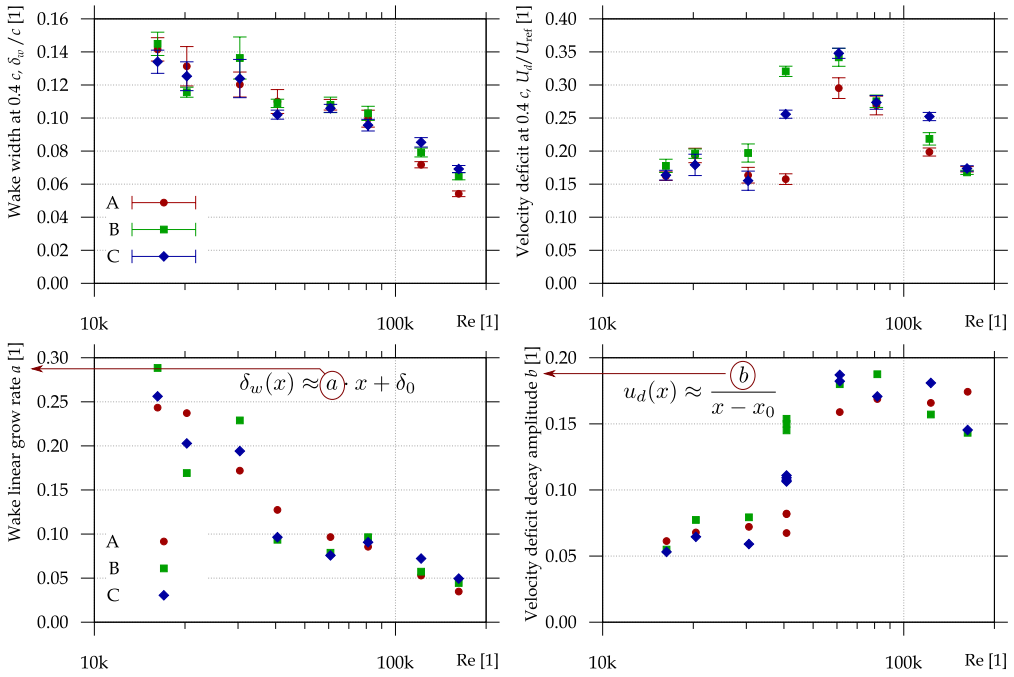

Figure 12. (Top left) Dependence of the wake width δ_w at fixed stream-wise distance $x = 0.4c$ past the trailing edge on the chord-based Reynolds number. (Top right) Dependence of the velocity deficit at certain distance $x = 0.4c$ on the Reynolds number. (Bottom left) Dependence of the grow rate of the wake width a on the Reynolds number. (Bottom right) decay rate of velocity deficit, if a hyperbolic decrease is expected. Angle of attack $\alpha = 0°$ in all panels.

airfoil: at the smaller Reynolds number, the turbulent structures are large and oriented with the height of the airfoil, at large Reynolds numbers, the turbulent structures might be small and isotropically oriented, thus the planar definition of TKE would contain approximately 2/3 of the true TKE. Another important note is, that the velocity $\vec{u}(\vec{x})$ is already averaged over the interrogation area – it is not a true single-point quantity. Therefore, the entire amount of TKE of length-scales smaller than the interrogation area is missing.

Figure 13 shows the spatial distribution of TKE based on two measured velocity components. The first impression is the decrease of $\mathrm{TKE}/U_{\mathrm{ref}}^2$ with Reynolds number (note the colorscale of the last row of Figure 13 is multiplied by 8). The worst product A creates significantly smaller amount of TKE, mainly at largest Re. An regime switch can be observed at Reynolds number $4.08 \cdot 10^4$, where the variant A lies in the previous stage with a single massive spot of TKE, while B and C wakes consist of a pair of maxima past the boundary layers.

This change of regime is even better apparent in the plot of $\sigma[v]/\sigma[u]$ in Figure 15. In respect to the original work of Romano [37], the logarithm is used in order to make the anisotropy symmetrical, because the logarithm maps the interval $(0, \infty)$ with center in 1 to interval $(-\infty, \infty)$ with center in 0. Thus the areas, where fluctuations in both investigated directions are statistically same, have got value around 0 plotted as white color; the areas, where the fluctuations in cross-stream directions are twice stronger than in the stream-wise direction, have got the value $+1$ and they are depicted by a blue color.

At smaller Re, the strong dominance of fluctuations in cross-stream direction is observed. This is caused by the von Kármán vortex street formed past the airfoil. The areas at the left-hand-side of the FoV, but not behind the airfoil, where the stream-wise fluctuations dominate, can be caused by the unsteadiness of the wind tunnel velocity, which is a known issue at smaller velocities. This fluctuations occur in the stream-wise direction only.

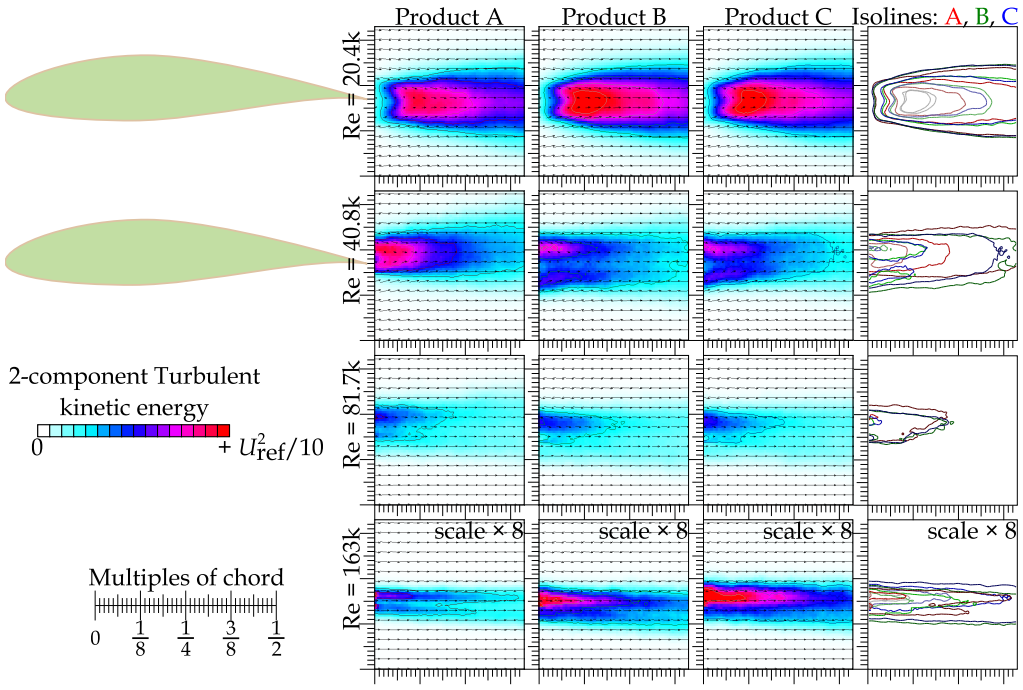

Figure 13. Turbulent kinetic energy (TKE) based on in-plane velocities only (thus it is though to be underestimated) obtained behind three different manufactured samples denoted A, B and C. The scale is adapted to $\frac{1}{10}U^2_{\text{ref}}$ except for the last line, where the scale is $\frac{1}{80}U^2_{\text{ref}}$. Angle of attack $\alpha = 0°$ in all panels.

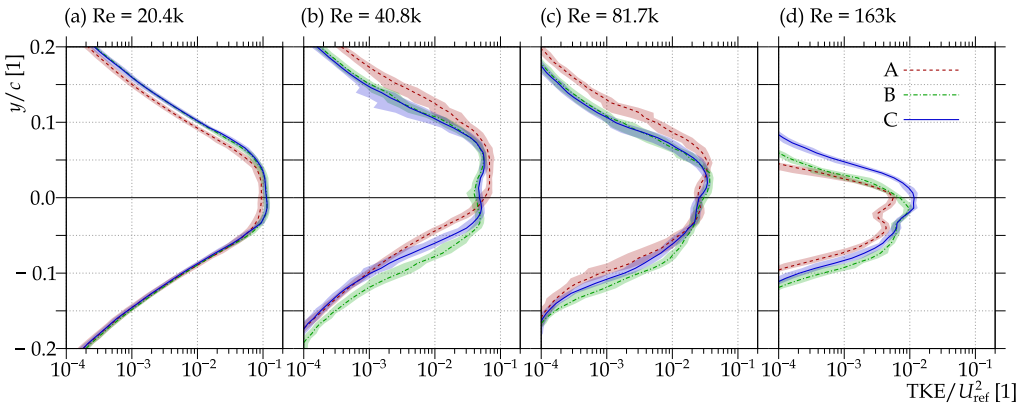

Figure 14. The cross-stream profile of the turbulent kinetic energy (TKE) at stream-wise distance 10 mm $= 1/8c$ past the trailing edge. Angle of attack $\alpha = 0°$ in all panels. Note the logarithmic scale!

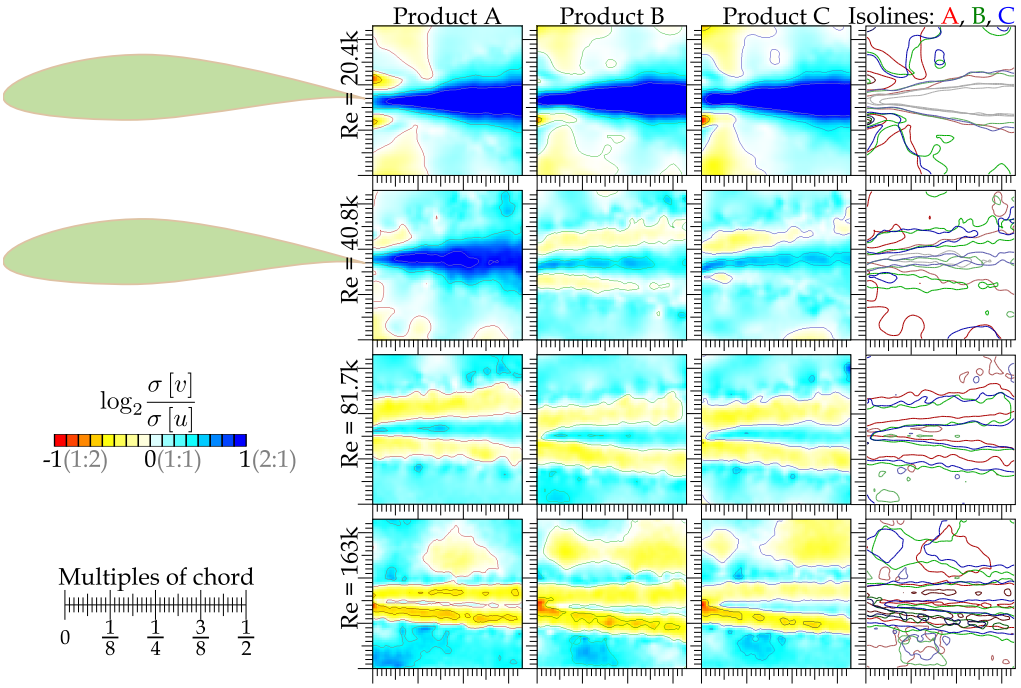

Figure 15. Panels (a - c) show the ratio of cross-stream fluctuations to stream-wise fluctuations obtained behind three different manufactured samples denoted A, B and C. Angle of attack $\alpha = 0°$ in all panels. Redder colors signify dominance of stream-wise fluctuations, which is typical for areas of continuing boundary layer, while the bluer colors highlight areas of stronger cross-stream fluctuations, which is typical for the so-called *true wake*.

At $\mathrm{Re} = 4.04 \cdot 10^4$, the regime changes in favor to the stream-wise fluctuations. However, there is a central strip of cross-stream fluctuations dominance, which is connected with the von Kármán vortex street, which is still present at those velocities. The central blue strip weakens with increasing Reynolds number, but it still exists at the largest explored velocity.

The dominance of stream-wise fluctuations is caused by the continuation of boundary layers formed along the airfoil. The length-scale of a fluctuation inside boundary layer is limited in cross-stream direction by the thickness of the boundary layer, while the stream-wise fluctuations are not limited in their development. The level of anisotropy becomes stronger at the pressure side of the airfoil (bottom part of the figures) and at the largest explored Re.

The classical approach of investigating anisotropy [38] uses all three instantaneous velocity components measured at least in single point by 3-wire Hot Wire Anemometer [39] or by using Stereo PIV [40–42]. In this experiment, we have only two velocity components, although Stereo-PIV measurement is *planned to the future*. In the case of 2D velocity components, the eigen values cannot be extracted, thus we are limited to the ratio of fluctuations in two directions, which is already used in article by Romano [37]. Another approach is to use the so-called *degree of anisotropy*, where the difference plays a role instead of the ratio, as it is used e.g. in the book [43]. The spatial distributions obtained by using the *degree of anisotropy* or by using the ratio of $\sigma[v]/\sigma[u]$ are very similar.

3.6. TKE by length-scale of fluctuations

A better insight into the nature of turbulent kinetic energy can be achieved by looking, which are the sizes of fluctuations producing the TKE [1]. This can be done by using our approach [24,44] of separating the fluctuations by length-scale inspired by the work of Agrawal and Prasad [45,46]. The spatial spectrum [24] is obtained without a

need of temporal resolution [47]. The idea is quite simple: spatially resolved velocity field $\vec{u}(\vec{x})$ is convoluted with a band-pass-filter:

$$\vec{u}_{lh}(\vec{x}) = \vec{u}(\vec{x}) * P_{lh}(\vec{x}), \tag{7}$$

where $P_{lh}(\vec{x})$ is the band-pass-filter keeping structures of size larger than σ_l and smaller than σ_h. It is obtained as a difference of two Gauss functions:

$$P_{lh}(\vec{x}) = \frac{1}{2\pi\sigma_l^2} e^{-\frac{x^2}{2\sigma_l^2}} - \frac{1}{2\pi\sigma_h^2} e^{-\frac{x^2}{2\sigma_h^2}}. \tag{8}$$

Then, the spatial distribution of turbulent kinetic energies of different bands $\vec{u}_{lh}(\vec{x})$ is calculated. Figure 16 displays combination of spatial distributions of TKE of three bands depicted by three basic colors: red for the TKE of spatially smallest fluctuations of length interval $1.0 - 1.5$ grid points, which corresponds to $7 \cdot 10^{-3} - 1 \cdot 10^{-2} c$, c chord width. The green channel shows fluctuations of length interval $3 - 4$ grid points, i.e. $(2.0 - 2.7) \cdot 10^{-2} c$ and the blue colors represent the largest resolved fluctuations of sizes between $8 - 12$ grid points, i.e. $(5.3 - 8.0) \cdot 10^{-2} c$. The relative intensities $\hat{I}(k)$ of each color channel have to be normalized according to the band interval $k/\Delta k^2$. Additionally, it is normalized by the famous Kolmogorov scaling [48] $k^{-5/3}$ in order to get equal color intensities in the case, when the power spectral density follows this scaling;

$$\hat{I}(k) \sim E_T(k) \cdot \frac{k}{\Delta k^2} \cdot k^{\frac{5}{3}}, \tag{9}$$

where the effective wave number of an explored band of fluctuations with the size between σ_l and σ_h is calculated as

$$k = \frac{2}{\sigma_l + \sigma_h} \tag{10}$$

and

$$\Delta k = \frac{1}{\sigma_l} - \frac{1}{\sigma_h}. \tag{11}$$

By using more bands within the spatial resolution of our data, the spatial power spectral density $E(k)/k$ can be reconstructed. It is important to note, that in respect to the classical spectra obtained from time-resolved point data (e.g. [49–51]), our method is limited to the range of field of view to the grid point. This interval covers only values from 0.53 mm to 32 mm, i.e. one and half orders of magnitude. The classical time resolved point measurements typically cover tens of minutes by resolution of tens of kilohertz covering five orders of magnitude in frequency [52]. Our approach shows the spectra calculated by using the entire field of view, each point is affected by all other points in the data ensemble. Moreover, the signal by larger scales feels larger neighboring, while the smallest scale signal is almost local.

The spatial distribution of length-scale dependent TKE is shown in Figure 16. At lower Re, there are large areas displaying relative large-scale source of TKE, which is displayed as a massive blue spot. This is caused by large almost laminar vortices in the forming von Kármán vortex street. At Re $4.08 \cdot 10^4$, the wake past the product A belongs rather to the previous regime, while the others to the next regime characterized by continuing boundary layers containing small scale fluctuations. The wake is still affected by larger scale oscillations of the wake, thus it is displayed in violet colors – it contains large scales and small scales, the middle scales are depleted. At even higher Re, the importance of large-scales decreases, and the asymmetry appears between the pressure and suction side of the wake – there is more middle scale fluctuations (green) past the pressure side. At the highest explored Re $1.63 \cdot 10^5$, the large-scales are weaker, the wake consists of a pair of strips of middle- and small-scale fluctuations (yellow)

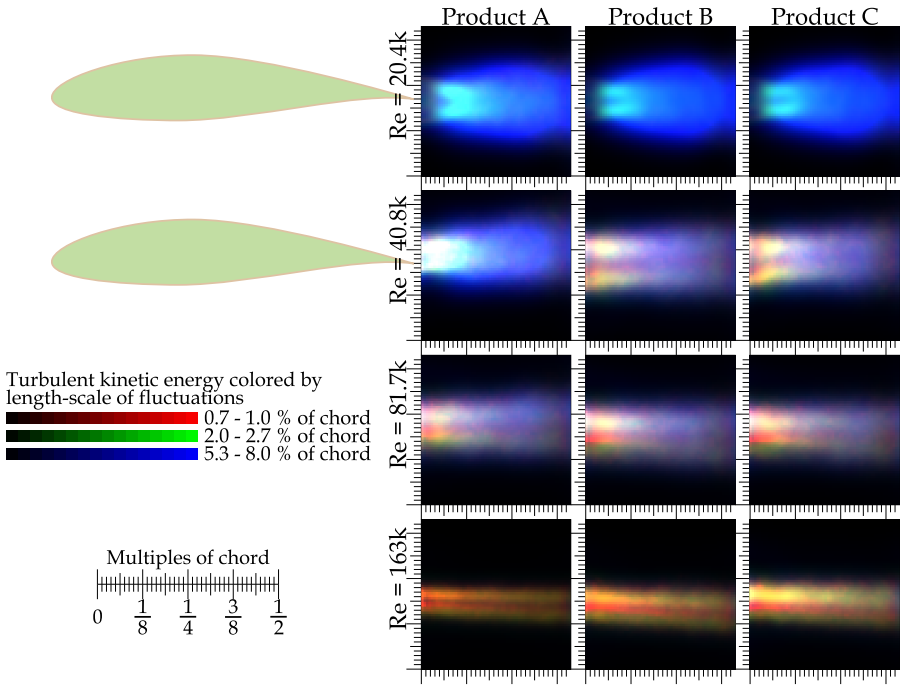

Figure 16. Turbulent kinetic energy colored by the length-scale of fluctuations producing it at angle of attack $\alpha = 0°$. TKE is divided into three channels: red channel represents fluctuations of size $0.7 - 1.0\%$ of chord width, green channel shows fluctuations of size between 2.0% and 2.7% of chord width, while the blue plays for the largest fluctuations of size $5.3 - 8.0\%$ of chord. The colorscale among different color channels is normalized in such a way, that an ideal Kolmogorov turbulence would be displayed in shades of gray. Among different Re and variants, the colorscale is automatically adapted (for differences in amount of TKE look to Figure 13 or Figure 14).

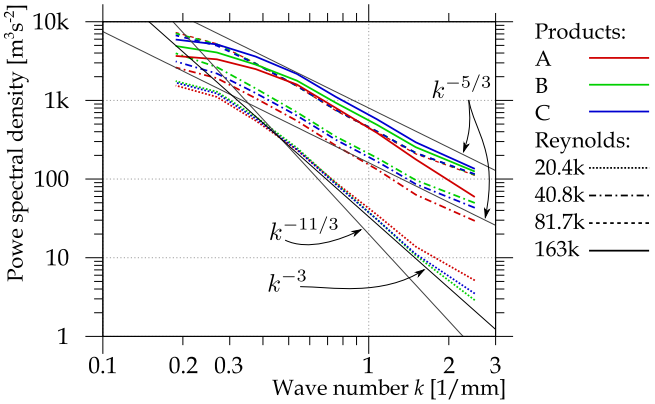

Figure 17. Spatial spectra of turbulent kinetic energy. The different products are distinguished via color, the Reynolds number via line style angle of attack is zero in all cases. Thin lines represent scalings: $k^{-5/3}$, k^{-3} and $k^{-11/3}$.

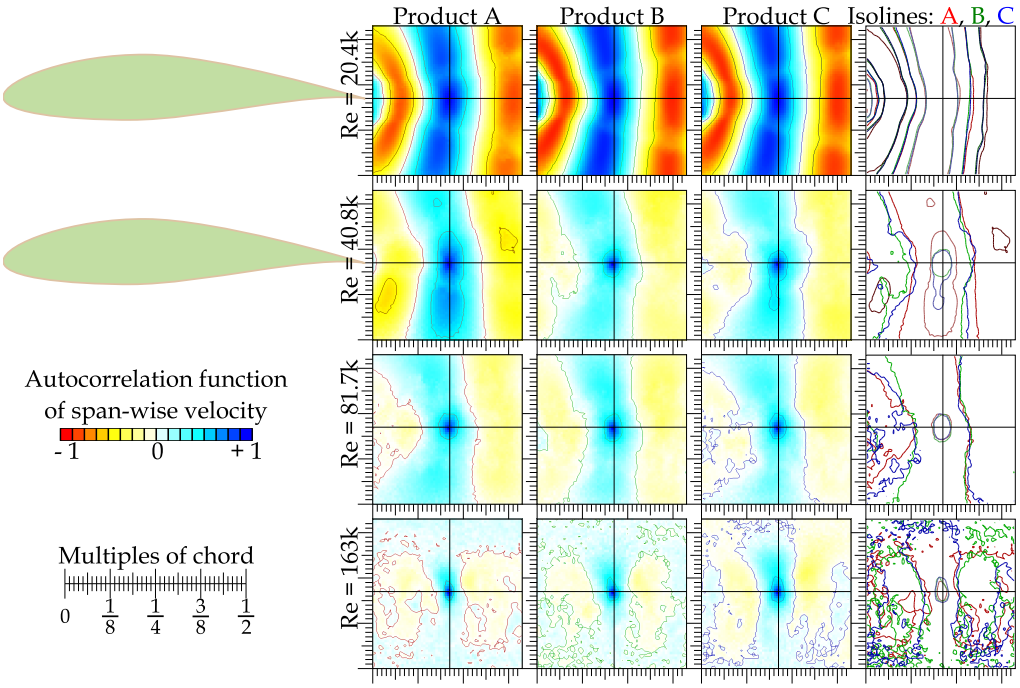

Figure 18. Autocorrelation function of cross-stream velocity component v with a reference point in the middle of the field of view, i.e. $0.21c$ past the trailing edge at $\alpha = 0°$.

with a strip of small scales (red) in between. Lets mention again, that the dominance of some color in Figure 16 signifies, that there is slightly more energy in corresponding length-scale-band, than it would be in the case of ideal turbulence following 5/3 law. Therefore, the energy content of large-scale fluctuations at the highest Reynolds number is still larger than the two other band combined in absolute numbers. This issue is better apparent in the plot of power spectral density in Figure 17.

The power spectral density, Figure 17, displays k^{-3} scaling at the smallest Re. Lets mention, that even steeper scaling $k^{-11/3}$ is typical for two dimensional arrangement of vortices [53], which is typically observed in low-Reynolds number wake past circular cylinder. At higher Reynolds numbers, the spectra approaches the $k^{-5/3}$ law. Note, that the vertical axis is not normalized by U_{ref}^2; it displays absolute numbers. Despite this, the wake at Re $1.63 \cdot 10^5$ displays less large-scale energy than wake at Re $8.2 \cdot 10^4$, while at middle- and small-scale wave numbers, the larger Re contains more energy.

3.7. Spatial correlation

Another way of exploring the size of turbulent structures is the usage of the autocorrelation functions or the structure functions [54,55]. Here, the autocorrelation function of cross-stream velocity component is used, because this component is active in the formation of von Kármán vortex street observed at the lower Reynolds numbers. The autocorrelation of some quantity between two separate points $\vec{x}$ and $\vec{\xi}$ is defined as

$$R_{vv}\left(\vec{x};\vec{\xi}\right) = \frac{\left\langle v'(\vec{x}) \cdot v'\left(\vec{\xi}\right)\right\rangle}{\sigma[v(\vec{x})] \cdot \sigma\left[v\left(\vec{\xi}\right)\right]}, \tag{12}$$

where $\langle \cdot \rangle$ signifies the ensemble averaging and $\sigma[\,\cdot\,]$ is the standard deviation; v' is a fluctuation velocity, $v' = v - \langle v \rangle$. In Figure 18, the position vector $\vec{x}$ runs over the entire FoV, while the reference point $\vec{\xi}$ is fixed in the FoV center.

One of the natural properties of correlation function is, that it inherits some aspects of the basic function, e.g. its periodicity. Therefore, the periodic von Kármán vortex

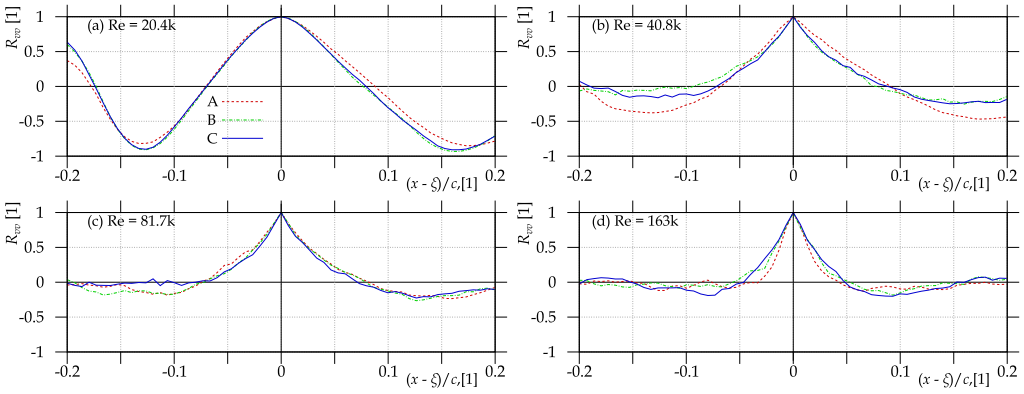

Figure 19. The stream-wise profile of the autocorrelation function of cross-stream velocity component at $\alpha = 0°$.

street is reflected as a periodic function of autocorrelation with minima in the distance of half of the spatial period. Note that the distance of minimum is shorter in upstream direction and longer in downstream direction (e.g. at Re $1.63 \cdot 10^4$, Figure 19(a), the minimum in upstream direction occurs distance at $-0.15c$ for the case A and at $-0.13c$ for B and C, while in the upstream direction, the first minimum is $0.18c$ for A and 0.17 for B and C). With increasing Re, the dominant periodic behavior disappears and the R_{vv} starts to represent the spatial decay of coherence.

The level of spatial coherence is characterized by the integral length-scale, which is defined as the integral of R_{vv} up to some distance M, where R_{vv} reaches zero, $R_{vv}(M) = 0$

$$L_{vv} = \int_0^M R_{vv}(x - \xi)\mathrm{d}x. \tag{13}$$

But reaching zero is not straight-forward as all experimental data contain noise. Thus the autocorrelation oscillates around zero, see Figure 19 later panels. Azevedo et al. [56] explores several possibilities of limits of this integral. Here, the simplest key is chosen: the integration is stopped in the distance, where R_{vv} reaches value $1/e \approx 0.367$. This choice underestimates the integral length-scale, as it is shown in [56], but it does it in a most systematic way.

The values of integral length-scales integrated up to the distance, where $R_{vv}(x) = 1/e$, are plotted in Figure 20. The panel (a) of Figure 20 shows L_{vv} along the stream-wise direction in millimeters. L_{vv} decays systematically and continuously with increasing Re. Note that the interpretation of L_{vv} depends on the regime: at the periodic regime, where R_{vv} is a periodic function with the period of Strouhal shedding, it might represent just a constant fraction of spatial Strouhal period[2]. At regime dominated by continuing boundary layers, L_{vv} might represent the statistical size of coherent structures, which is the original motivation for this quantity. But, a systematic shortening of L_{vv} is observed without some evidence of regime change. However, if L_{vv} is calculated along the cross-stream direction (panel (c) in Figure 20), the switch of regimes is evident. At lower Reynolds number, the observed L_{vv} along cross-stream direction is as large as the measured area. When the large von Kárm'an street disappears, the value of L_{vv} along cross-stream direction converges to the range observed along stream-wise direction (panel (a) of Figure 20). The lost of large-scale vertical correlation appears at the already discussed regime change at Re $= 4.04 \cdot 10^4$.

The autocorrelation function R_{vv} is not symmetric between upstream and downstream direction, as it is shown in the panel (b) of Figure 20. The asymmetry reaches

[2] suppose that $R_{vv} = \cos ax$, where a is 2π times the spatial Strouhal frequency, then $L_{vv} = \left[a^{-1} \sin x\right]_0^M$, where $M, R_{vv}(M) = e^{-1}$, thus $M = a^{-1} \arccos e^{-1}$. Rewrite $\sin x = \sqrt{1 - \cos^2 x}$, then $L_v v = a^{-1} \sin \arccos e^{-1} = a^{-1}\sqrt{1 - e^{-2}} = 0.923a^{-1}$.

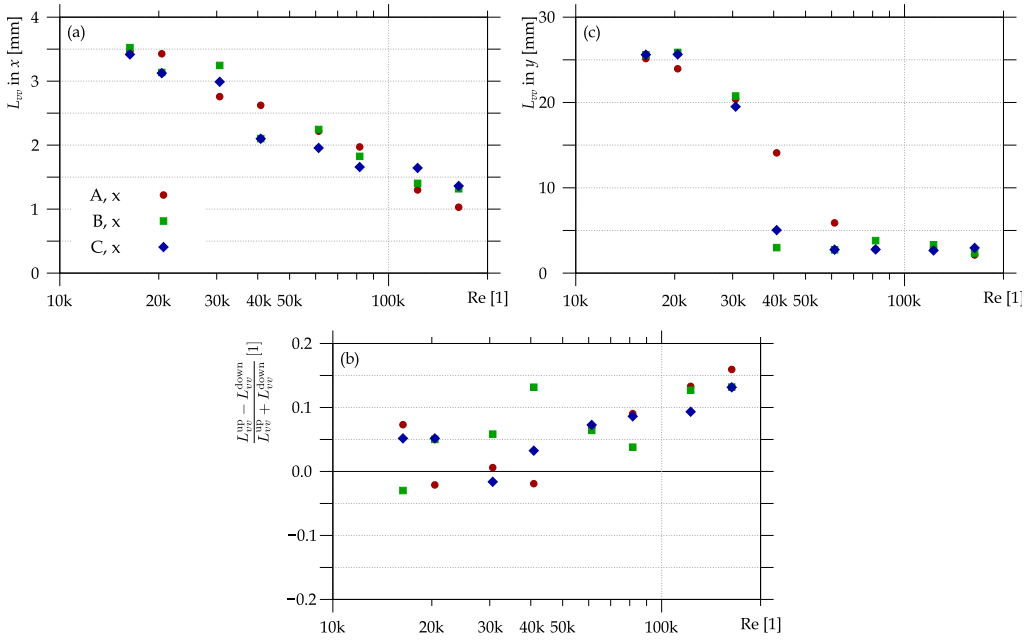

Figure 20. Integral length-scale of cross-stream velocity component v. Panel (a) shows the integral length-scale along stream-wise axis, however it is different in up-stream and down-stream direction, therefore panel (b) shows this asymmetry. Panel (c) shows the integral length-scale of v along cross-stream axis. Angle of attack $\alpha = 0°$ in all panels.

the values of 15% in favor of the downstream direction. This effect is caused by the increasing average velocity along the stream, as the wake widens.

4. Conclusion

We asked, how the manufacturing inaccuracies affect the flow topology. The wake behind a single prismatic airfoil NACA 64(3)-618 has been studied experimentally by using the Particle Image Velocimetry (PIV) method. The airfoil has been realized in three copies of different similarity to the ideal model. The real geometry has been measured by using 3D optical scanner GOM Atos. We focused to the zero angle of attack at chord-based Reynolds number ranging from $1.6 \cdot 10^4$ to $1.6 \cdot 10^5$.

Generally speaking, the effect of model quality is weaker than the effect of Reynolds number – the average flow pattern differs more among different velocities than among different models. The deviations in model shape shifts the transition between turbulent regimes, which is best observable at Reynolds number $4.1 \cdot 10^4$, where the variant denoted A displays same regime as for smaller velocities, while other two realizations B and C produces wake similar to that observable at higher velocities. This regime change is apparent in average flow topology (Figure 6), in the decrease of average velocity deficit (Figure 12), in the spatial distribution of turbulent kinetic energy (Figure 13), in the analysis of isotropy (Figure 15) or in the length-scale of structures producing TKE (Figure 16). This issue can be important, if the flow machine (e.g. wind turbine) was designed to operate at edge of some regime.

The worst variant A differs from the ideal geometry mainly in the quality of trailing edge: it is shorter by 2.8 mm (3.5% of the chord length), it lacks the entire small trail pointing to the pressure side of the airfoil, see Figure 1. Thus it produces smallest lift (Figure 8), but also the smallest drag (Figure 9), as the other variants are slightly expanded by using Minkowski sum. Despite this huge discrepancy, the flow characteristics of this realization are *comparable* to the better models. The wake centerline orientation is similar to others (Figure 10), the wake thickness reaches similar values (Figure 12), and

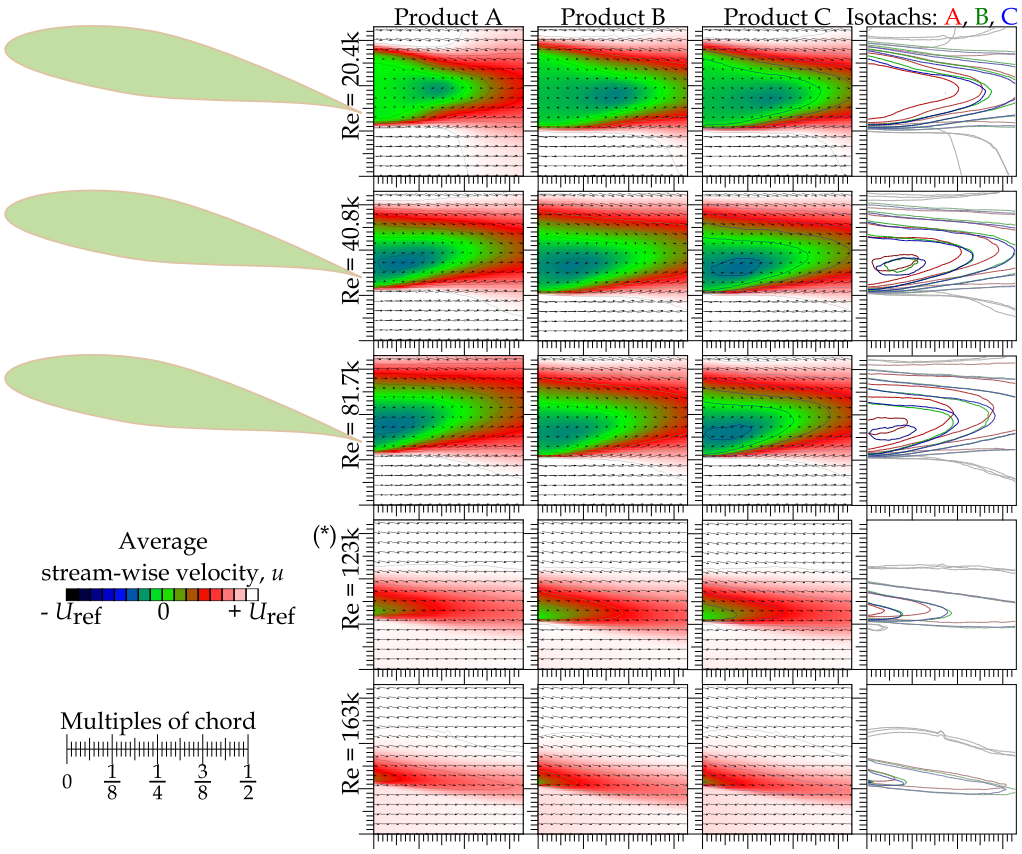

Figure A21. Map of ensemble average of stream-wise velocity u at angle of attack $\alpha = 10°$. In respect to Figure 5, here is an added row denoted (*) containing data at $\mathrm{Re} = 1.23 \cdot 10^5$ in order to show that the flow is adhered at this velocity.

even the length-scales of fluctuations in the wake display similar pattern (Figure 16) and spectrum (Figure 17) as better brothers.

In the future, we plan to compare these results with numerical simulation covering not only the scanned geometry, but also the ideal design, which is not accessible by the experiment.

Appendix E Large angle of attack

Increasing the angle of attack can, generally, increase the lift coefficient even at symmetrical airfoils. But it works only up to a critical angle, where the stall occurs. In this study, we measured only at angles $0°$ and $+10°$, which is quite a large angle. The separation bubble is well resolvable in the plots of ensemble average stream-wise velocity in Figure A21. The critical velocity of stall has been not measured at certain α, neither the critical angles of stall were explored at certain velocity. The only information, which can be read out of our data is, that at $\alpha = +10°$ the stall critical Reynolds number lies between $8.17 \cdot 10^4$ and $1.23 \cdot 10^5$.

Similarly, the wake centerline points towards the pressure side of the airfoil since $\mathrm{Re} = 1.23 \cdot 10^4$, at lower velocities, it points towards the suction side (up in images). The centerline is determined as set of points, where $\mathrm{d}\langle u \rangle / \mathrm{d}y = 0$, which highlights minima as well as maxima of the cross-stream velocity profiles, see Figure A22.

The difference among airfoil variants is best visible in the plot of TKE in Figure A23. The flow past variant A at Reynolds number $2.04 \cdot 10^4$ displays clearly a different regime than the flow past B and C variants. As discussed above, this discrepancy could be caused by the slightly smaller size of A and thus slightly smaller *true* Re. Thus in Figs. A23 and A24, one row is plotted in advance; that row contains data at even smaller

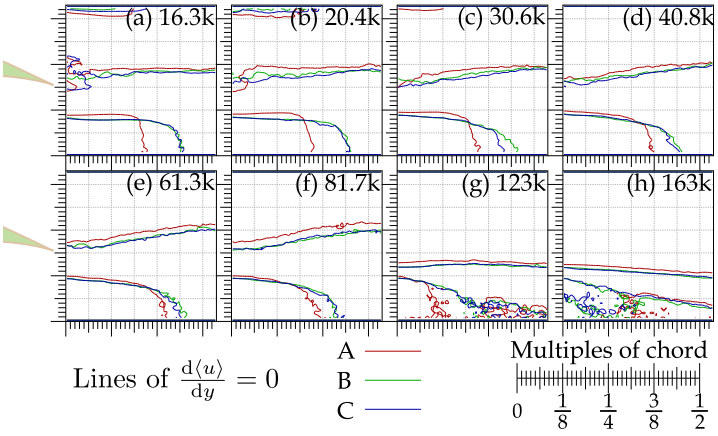

Figure A22. Lines of extrema of $\langle u \rangle$ along cross-stream direction (y). The number in top right corner of each panel is chord-based Reynolds number and k denotes $\cdot 10^3$. Angle of attack $\alpha = 0°$ in all panels.

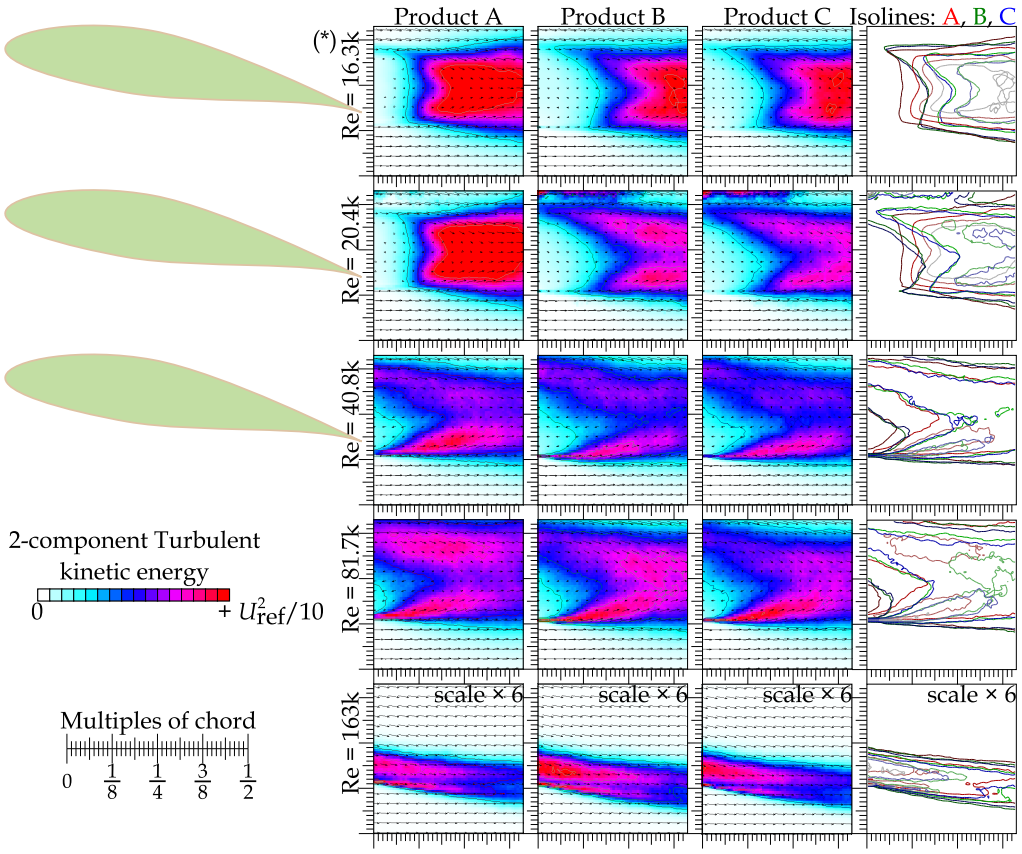

Figure A23. Map of turbulent kinetic energy at angle of attack $\alpha = 10°$. The first row is added, it is denoted (*) and it contains data at $\mathrm{Re} = 1.63 \cdot 10^4$ in order to show that the wake past product A at $\mathrm{Re} = 2.04 \cdot 10^4$ belongs to previous regime.

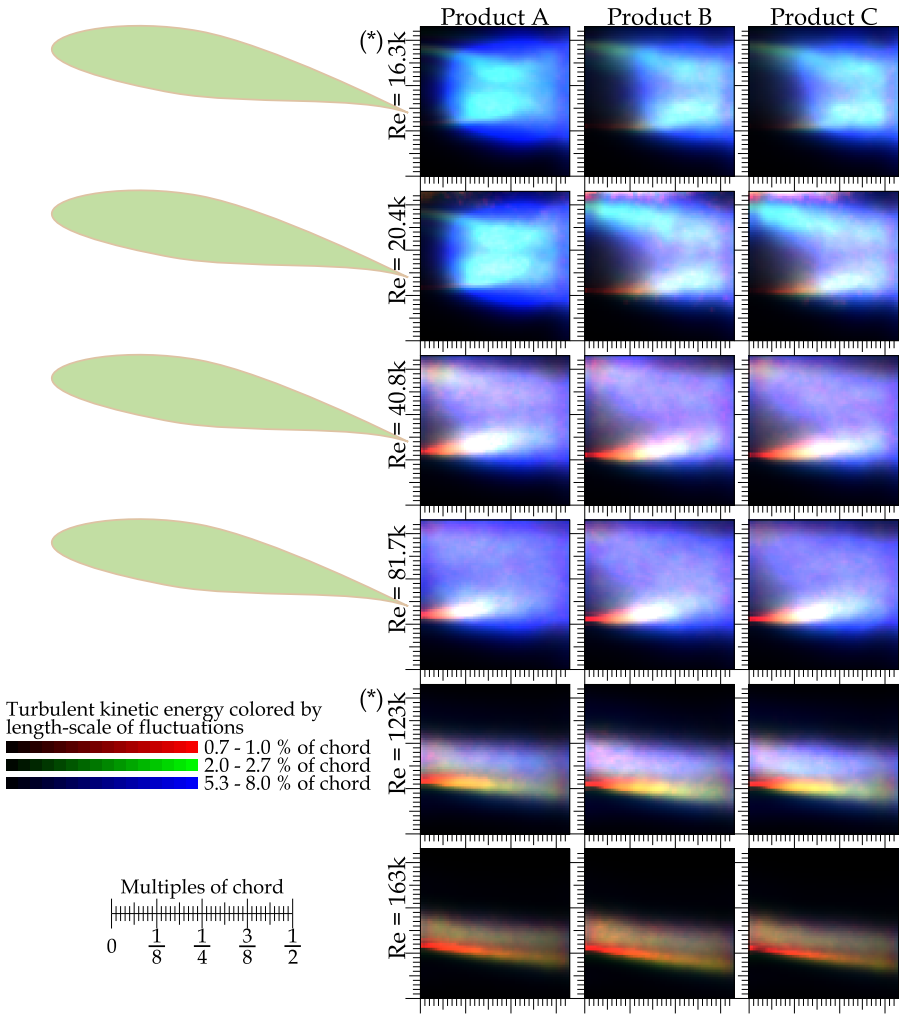

Figure A24. Turbulent kinetic energy colored by the length-scale of fluctuations producing it. TKE is divided into three channels: red channel represents smallest length-scale of fluctiations, green channel shows fluctuations of middle sizes, while the blue plays for the largest fluctuations. The colorscale among different color channels is normalized in such a way, that an ideal Kolmogorov turbulence would be displayed in shades of gray. Among different Re and variants, the colorscale is automatically adapted (for differences in amount of TKE look to Figure A23. Rows denoted by (*) are added.

Reynolds number of $1.63 \cdot 10^4$. The topology of the wake past product A at $\mathrm{Re} = 2.04 \cdot 10^4$ is more similar to the wake past all variants at $\mathrm{Re} = 1.63 \cdot 10^4$. However, the plot of length-scale dependent TKE (Figure A24) reveals the difference between A and B, C even at smallest explored Reynolds number – wakes past all products are dominated by the largest length-scale at this Re; but the products B and C contain slightly larger amount of middle-scales and the maxima are better separated than past the A variant.

At Re between 4.1 and $8.2 \cdot 10^4$, the wake contains small-scale fluctuations in its pressure side (bottom part of figures), while in the suction side (upper in figures), it contains mostly fluctuations of larger scales being depleted by small scales, because the shear layer turbulence is *elder* here (the flow is detached close to the leading edge, then it develops dissipating energy at smallest scales due to the viscosity. Therefore, the smallest scales are depleted first). Thus the upper shear layer in Figure A24 is less localized and constructed by fluctuations of larger scales.

At $\mathrm{Re} = 1.23 \cdot 10^5$, the flow is attached, as it has been discussed above and shown in Figure A21, but still the suction side of the wake contains significantly stronger signal

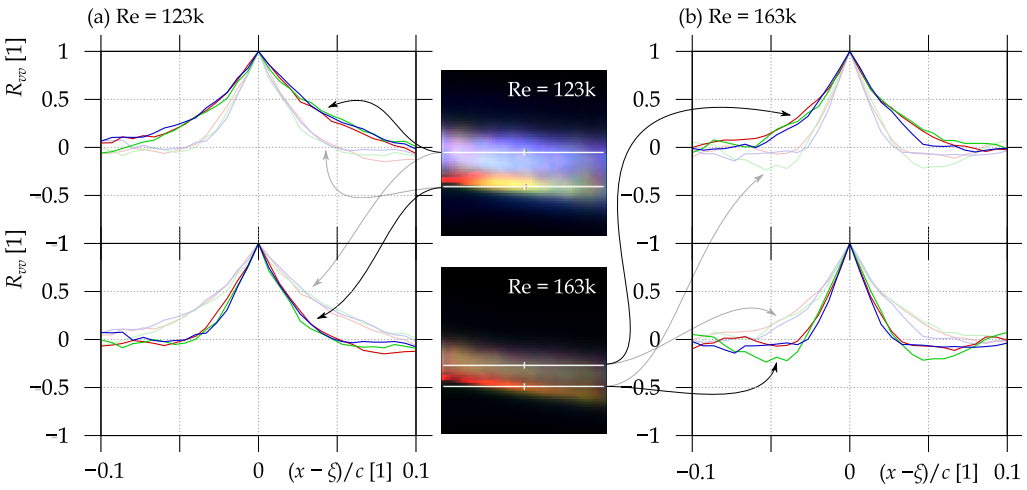

Figure A25. Autocorrelation function of fluctuating cross-stream velocity component v at two Reynolds numbers $1.23 \cdot 10^5$ (a,b) and $1.63 \cdot 10^5$ (c,d), where the flow is attached at $\alpha = 10°$. First, the autocorrelation with reference point in the suction part of the wake (top) and second with reference point in the pressure part of the wake (bottom).

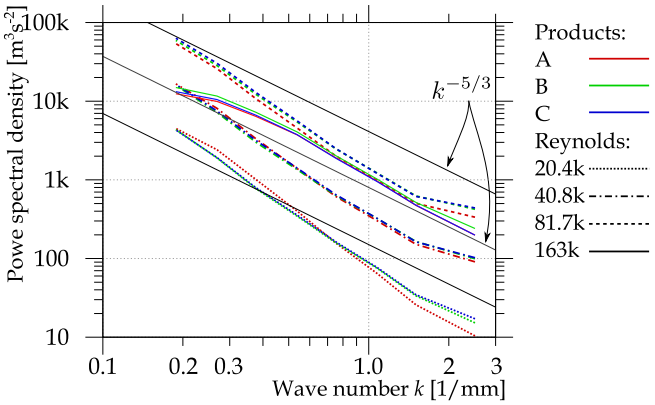

Figure A26. Spatial spectrum of the turbulent kinetic energy at $\alpha = 10°$. Products are distinguished via colors, Reynolds number are by different linestyles. The thin black lines represent the $k^{-5/3}$ scaling.

from large-scale fluctuations, because the boundary layer at suction side (top) is less stable than at pressure side (bottom). At even higher Reynolds number, the boundary layer is more stable and the wake does not contain large-scale (blue) signal any more, however, there is an asymmetry between pressure and suction side. The autocorrelation function in Figure A25 shows the same – the coherent structures are significantly larger inside the suction part of the wake than in the pressure part. The different airfoil variants follow more or less the same pattern. only the variant B displays stronger periodic behavior at $\mathrm{Re} = 1.63 \cdot 10^5$ in the autocorrelation with reference point in the pressure part of the wake, see Figure A25(d).

The spatial spectra, whose construction has been shortly described above or in more details in our previous publication [24], is plotted in Figure A26 for the angle of attack $\alpha = 10°$. There is visible the contrast between the adhered flow at $\mathrm{Re} = 1.63 \cdot 10^5$ (displayed by solid lines) and the smaller velocities with stall. The largest Re contains less energy at largest scales, than the flow at *four times* smaller velocity! At middle scales, it contains comparable amount of energy as the flow at half the velocity. The power spectral density is steeper than the Kolmogorov scaling, except for the largest k, where

the instrumental noise appears. This scaling is even steeper at larger scales (which is not valid for the largest Re).

Appendix F Acknowledgment

We thank to Jaroslav Synáč for discussion about geometry modifications, to Petr Eret for maintaining the project and to Jan Narovec for help during the PIV measurement.

The work was supported from ERDF under project „Research Cooperation for Higher Efficiency and Reliability of Blade Machines (LoStr)“ No. CZ.02.1.01 / 0.0 / 0.0 / 16_026 / 0008389.

The article processing fee has been paid by European Union, as part of the project entitled Development of capacities and environment for boosting the international, intersectoral and interdisciplinary cooperation at UWB, project reg. No. CZ.02.2.69 / 0.0 / 0.0 / 18_054 / 0014627.

References

1. Frisch, U.; Kolmogorov, A.N. *Turbulence: the legacy of AN Kolmogorov*; Cambridge university press, 1995.
2. AIAA. *Guide for the Verification and Validation of Computational Fluid Dynamics Simulations*; G-077, AIAA, 1998. doi:10.2514/4.472855.001.
3. Drela, M. Airfoil Tools. http://airfoiltools.com. Accessed: 2021-04-20.
4. Moreno-Oliva, V.I.; Román-Hernández, E.; Torres-Moreno, E.; Dorrego-Portela, J.R.; Avendaño Alejo, M.; Campos-García, M.; Sánchez-Sánchez, S. Measurement of quality test of aerodynamic profiles in wind turbine blades using laser triangulation technique. *Energy Science and Engineering* **2019**, *7*, 2180–2192. doi:10.1002/ese3.423.
5. Drela, M. XFOIL: An Analysis and Design System for Low Reynolds Number Airfoils. *LOW REYNOLDS NUMBER AERODYNAMICS.PROC.CONF., NOTRE DAME, U.S.A., JUNE 5-7, 1989* **1989**, *54*, 1–12. doi:10.1007/978-3-642-84010-4.
6. Ravikovich, Y.; Kholobtsev, D.; Arkhipov, A.; Shakhov, A. Influence of geometric deviations of the fan blade airfoil on aerodynamic and mechanical integrity. Journal of Physics: Conference Series, 2021, Vol. 1891, p. 012042. doi:10.1088/1742-6596/1891/1/012042.
7. Klimko, M.; Okresa, D. Measurements in the VT 400 air turbine. *Acta Polytechnica* **2016**, *56*, 118. doi:10.14311/AP.2016.56.0118.
8. Uher, J.; Milcak, P.; Skach, R.; Fenderl, D.; Zitek, P.; Klimko, M. Experimental and Numerical Evaluation of Losses From Turbine Hub Clearance Flow. Turbo Expo: Power for Land, Sea, and Air, 2019, Vol. Volume 2B: Turbomachinery, p. 9. doi:10.1115/GT2019-90726.
9. Winstroth, J.; Seume, J.R. On the influence of airfoil deviations on the aerodynamic performance of wind turbine rotors. Journal of Physics: Conference Series, 2016, Vol. 753. doi:10.1088/1742-6596/753/2/022058.
10. Alsoufi, M.S.; Elsayed, A.E. Surface Roughness Quality and Dimensional Accuracy - A Comprehensive Analysis of 100Cost-Effective FDM 3D Printer. *Materials Sciences and Applications* **2018**, *09*, 11–40. doi:10.4236/msa.2018.91002.
11. Inkinen, S.; Hakkarainen, M.; Albertsson, A..; Södergøard, A. From lactic acid to poly(lactic acid) (PLA): Characterization and analysis of PLA and Its precursors. *Biomacromolecules* **2011**, *12*, 523–532. doi:10.1021/bm101302t.
12. Zhang, C.; Zhao, H.; Gu, F.; Ma, Y. Phase unwrapping algorithm based on multi-frequency fringe projection and fringe background for fringe projection profilometry. *Measurement Science and Technology* **2015**, *26*. doi:10.1088/0957-0233/26/4/045203.
13. Li, F.; Stoddart, D.; Zwierzak, I. A Performance Test for a Fringe Projection Scanner in Various Ambient Light Conditions. Procedia CIRP, 2017, Vol. 62, pp. 400–404. doi:10.1016/j.procir.2016.06.080.
14. GOM, m. GOM Acceptance Test – Process Description, Acceptance Test according to the Guideline VDI/VDE 2634 Part 3, 2014.
15. Mendricky, R. Determination of measurement accuracy of optical 3D scanners. *MM Science Journal* **2016**, *2016*, 1565–1572. doi:{10.17973/MMSJ.2016.12.2016183}.
16. Vagovský, J.; Buranský, I.; Görög, A. Evaluation of measuring capability of the optical 3D scanner. Procedia Engineering, 2015, Vol. 100, pp. 1198–1206. doi:10.1016/j.proeng.2015.01.484.
17. Du, W.; Zhao, Y.; He, Y.; Liu, Y. Design, analysis and test of a model turbine blade for a wave basin test of floating wind turbines. *Renewable Energy* **2016**, *97*, 414–421. doi:10.1016/j.renene.2016.06.008.
18. Gom, m. ATOS Core. https://www.gom.com/en/products/3d-scanning/atos-core. Accessed: 2021-04-20.
19. Krein, M.; Šmulian, V. On Regularly Convex Sets in the Space Conjugate to a Banach Space. *Annals of Mathematics* **1940**, *41*, 556–583. doi:10.2307/1968735.
20. Yanovych, V.; Duda, D.; horáček, V.; Uruba, V. Research of a wind tunnel parameters by means of cross-section analysis of air flow profiles. *AIP Conference Proceedings* **2019**, *2189*. doi:10.1063/1.5138636.
21. Yanovych, V.; Duda, D. Structural deformation of a running wind tunnel measured by optical scanning. *Strojnicky Casopis* **2020**, *70*, 181–196. doi:10.2478/scjme-2020-0030.
22. Duda, D.; Yanovych, V.; Uruba, V. An experimental study of turbulent mixing in channel flow past a grid. *Processes* **2020**, *8*, 1–17. doi:10.3390/pr8111355.
23. Tropea, C.; Yarin, A.; Foss, J.F. *Springer Handbook of Experimental Fluid Mechanics*; Springer, Heidelberg, DE, 2007; p. 1557.
24. Duda, D.; Uruba, V. Spatial Spectrum From Particle Image Velocimetry Data. *ASME J of Nuclear Rad Sci.* **2019**, *5*. doi:10.1115/1.4043319.

25. Von Kármán, T. *Aerodynamics*; McGraw-Hill paperbacks : science, mathematics and engineering, McGraw-Hill, 1963.
26. Drela, M. Low-Reynolds Number Airfoil Design for the MIT Daedalus Prototype: A Case Study. *Journal of Aircraft* **1988**, *25*, 724–732.
27. Drela, M.; Giles, M. Viscous-Inviscid Analysis of Transonic and Low Reynolds Number Airfoils. *AIAA Journal* **1987**, *25*, 1347–1355.
28. Terra, W.; Sciacchitano, A.; Scarano, F. Aerodynamic drag of a transiting sphere by large-scale tomographic-PIV. *Exp. Fluids* **2017**, *58*. doi:10.1007/s00348-017-2331-0.
29. Terra, W.; Sciacchitano, A.; Scarano, F. Drag analysis from PIV data in speed sports. *Procedia Engineering* **2016**, *147*, 50–55. doi:10.1016/j.proeng.2016.06.188.
30. Ragni, D.; Oudheusden, B.W.; Scarano, F. Non-intrusive aerodynamic loads analysis of an aircraft propeller blade. *Experiments in Fluids* **2011**, *51*, 361–371. doi:10.1007/s00348-011-1057-7.
31. Oudheusden, B.W. PIV-based pressure measurement. *MEASUREMENT SCIENCE AND TECHNOLOGY* **2013**, *24*, 032001. doi:{10.1088/0957-0233/24/3/032001}.
32. Antonia, R.A.; Rajagopalan, S. Determination of drag of a circular cylinder. *AIAA Journal* **1990**, *28*, 1833–1834. doi:10.2514/3.10485.
33. Zhou, Y.; Alam, M.M.; Yang, H.; Guo, H.; Wood, D. Fluid forces on a very low Reynolds number airfoil and their prediction. *International Journal of Heat and Fluid Flow* **2011**, *32*, 329–339. doi:10.1016/j.ijheatfluidflow.2010.07.008.
34. Mohebi, M.; Wood, D.H.; Martinuzzi, R.J. The turbulence structure of the wake of a thin flat plate at post-stall angles of attack. *Experiments in Fluids* **2017**, *58*. doi:10.1007/s00348-017-2352-8.
35. Duda, D.; Yanovych, V.; Uruba, V. Wake Width: Discussion of Several Methods How to Estimate It by Using Measured Experimental Data. *Energies* **2021**, *14*, 4712. doi:10.3390/en14154712.
36. Eames, I.; Jonsson, C.; Johnson, P.B. The growth of a cylinder wake in turbulent flow. *Journal of Turbulence* **2011**, *12*, N39. doi:10.1080/14685248.2011.619985.
37. Romano, G.P. Large and small scales in a turbulent orifice round jet: Reynolds number effects and departures from isotropy. *International Journal of Heat and Fluid Flow* **2020**, *83*. doi:10.1016/j.ijheatfluidflow.2020.108571.
38. Lumley, J.L.; Newman, G. The return to isotropy of homogeneous turbulence. *J. Fluid Meach.* **1977**, *82*, 161–178. doi:10.1017/S0022112077000585.
39. Simonsen, A.J.; Krogstad, P.o. Turbulent stress invariant analysis: Clarification of existing terminology. *Phys. Fluids* **2005**, *17*, 088103. doi:10.1063/1.2009008.
40. Choi, K.; Lumley, J.L. The return to isotropy of homogeneous turbulence. *J. Fluid Meach.* **2001**, *436*, 59–84. doi:10.1017/S002211200100386X.
41. Duda, D.; Bém, J.; Yanovych, V.; Pavlíček, P.; Uruba, V. Secondary flow of second kind in a short channel observed by PIV. *European Journal of Mechanics, B/Fluids* **2020**, *79*, 444–453. doi:10.1016/j.euromechflu.2019.10.005.
42. Bém, J.; Duda, D.; Kovařík, J.; Yanovych, V.; Uruba, V. Visualization of secondary flow in a corner of a channel. AIP Conference Proceedings, 2019, Vol. 2189, pp. 020003–1–6. doi:10.1063/1.5138615.
43. Kundu, P.; Cohen, I.; Dowling, D. *Fluid Mechanics*, 6 ed.; Academic Press, 2016.
44. Duda, D.; Uruba, V. PIV of air flow over a step and discussion of fluctuation decompositions. AIP conference proceedings, 2018, Vol. 2000, p. 020005. doi:10.1063/1.5049912.
45. Agrawal, A. Measurement of spectrum with particle image velocimetry. *Experiments in Fluids* **2005**, *39*, 836–840. doi:10.1007/s00348-005-0018-4.
46. Agrawal, A.; Prasad, A. Properties of vortices in the self-similar turbulent jet. *Experiments in Fluids* **2002**, *33*, 565–577. doi:10.1007/s00348-002-0507-7.
47. Duda, D.; La Mantia, M.; Skrbek, L. Streaming flow due to a quartz tuning fork oscillating in normal and superfluid He 4. *Physical Review B* **2017**, *96*. doi:10.1103/PhysRevB.96.024519.
48. Kolmogorov, A.N. Dissipation of Energy in the Locally Isotropic Turbulence. *Proceedings of the Royal Society A: Mathematical, Physical and Engineering Sciences* **1991**, *434*, 15–17. doi:10.1098/rspa.1991.0076.
49. Jiang, M.T.; Law, A.W.K.; Lai, A.C.H. Turbulence characteristics of 45 inclined dense jets. *Environmental Fluid Mechanics* **2018**, pp. 1–28. doi:10.1007/s10652-018-9614-8.
50. Barenghi, C.F.; Sergeev, Y.A.; Baggaley, A.W. Regimes of turbulence without an energy cascade. *Scientific Reports* **2016**, *6*, 1–11, [1609.09705]. doi:10.1038/srep35701.
51. Harun, Z.; Abbas, A.A.; Lotfy, E.R.; Khashehchi, M. Turbulent structure effects due to ordered surface roughness. *Alexandria Engineering Journal* **2020**, *59*, 4301–4314. doi:10.1016/j.aej.2020.07.035.
52. Bourgoin, M.; Baudet, C.; Kharche, S.; Mordant, N.; Vandenberghe, T.; Sumbekova, S.; Stelzenmuller, N.; Aliseda, A.; Gibert, M.; Roche, P..; Volk, R.; Barois, T.; Caballero, M.L.; Chevillard, L.; Pinton, J..; Fiabane, L.; Delville, J.; Fourment, C.; Bouha, A.; Danaila, L.; Bodenschatz, E.; Bewley, G.; Sinhuber, M.; Segalini, A.; Örlü, R.; Torrano, I.; Mantik, J.; Guariglia, D.; Uruba, V.; Skala, V.; Puczylowski, J.; Peinke, J. Investigation of the small-scale statistics of turbulence in the Modane S1MA wind tunnel. *CEAS Aeronautical Journal* **2018**, *9*, 269–281. doi:10.1007/s13272-017-0254-3.
53. Kraichnan, R.H. Inertial ranges in two-dimensional turbulence. *Physics of Fluids* **1967**, *10*, 1417–1423. doi:10.1063/1.1762301.
54. Schulz-DuBois, E.O.; Rehberg, I. Structure Function in Lieu of Correlation Function. *Applied Physics* **1981**, *24*, 323–329.
55. Kubíková, T. The air flow around a milling cutter investigated experimentally by particle image velocimetry. AIP Conference Proceedings, 2021, Vol. 2323, pp. 030006–1–8. doi:10.1063/5.0041860.

56. Azevedo, R.; Roja-Solórzano, L.R.; Bento Leal, J. Turbulent structures, integral length scale and turbulent kinetic energy (TKE) dissipation rate in compound channel flow. *Flow Measurement and Instrumentation* **2017**, *57*, 10 – 19. doi:https://doi.org/10.1016/j.flowmeasinst.2017.08.009.